Geochemical investigation of the late Ordovician Bighorn Dolomite of western Wyoming

A Thesis submitted to the faculty of
San Francisco State University
In partial fulfillment of
the requirements for
the Degree

Master of Science

In

Geoscience

by

Andrew James Bays

San Francisco, California

December 2022

Certification of Approval

I certify that I have read Geochemical investigation of the Late Ordovician Bighorn Dolomite of western Wyoming by Andrew James Bays, and that in my opinion this work meets the criteria for approving a thesis submitted in partial fulfillment of the requirement for the degree (Master of Science in Geoscience at San Francisco State University.

Yadira Ibarra, Ph.D.
Assistant Professor,
Thesis Committee Chair

Petra Dekens, Ph.D.
Professor

Mary Leech, Ph.D.
Professor

Abstract

The Bighorn Dolomite of the Central Rockies and Great Plains is a Late Ordovician (Katian) dolostone that formed prior to the Late Ordovician glaciation and mass extinction. This study is primarily concerned with the Steamboat Point Member (~70 m thick), which contains cm-scale mottled fabrics passing through four distinct facies. I complete a geochemical survey, examining the relationship between facies changes and geochemical trends, in order to correlate the facies chemostratigraphically and construct a story about the changing depositional environments. Methods include facies observations and geochemical analyses of core C520 from Sheridan County Wyoming, including isotopic analysis of carbon, oxygen, and strontium; determination of concentrations of iron, manganese, and strontium; and facies interpretations. Carbon isotope, conodont, and facies changes data reveals the Steamboat Point Member contains the Fairview carbon isotope excursion of the Katian Stage. Trends in trace metals, when combined with inferred sea level, indicate dispersion of metals via ocean circulation. The introduction of burrowing organisms accompanies sea level rise, suggesting a eustatic driver for species migration. Textural and geochemical observations support a relative lack of diagenesis among carbon and oxygen; however, strontium shows evidence for significant post-depositional augmentation. Scanning electron microscopy (SEM) reveals abundant micrometer-scale hydrocarbon droplets throughout the dolomite crystals. The Steamboat Point Member experienced sea level rise and fall, which overprinted and affected the geochemistry, facies, and ecology. The climate oscillation of the Late Ordovician occurred a few million years after the Steamboat Point Member was deposited, linking eustatic instability to mass extinctions and glaciation.

Acknowledgements

Thank you to my thesis advisor, Yadi Ibarra, whose insight and guidance made this possible.

Thank you to the Department of Earth & Climate Science at San Francisco State University, the ARCS Foundation, the Karen Grove & Jay Ach Scholarship Fund, the Osher Foundation, GSA, USGS, and the Core Research Center in Denver.

Table of Contents

List of Tables

List of Figures

Introduction

The Upper Ordovician Bighorn Dolomite is a massive cliff-forming unit (~ 150 m thick) that extends across northwestern Wyoming with outcrops in Idaho, Montana, and South Dakota (Holland & Patzkowsky, 2012). The Ordovician Period (~ 485–444 Ma) oversaw a sharp increase in marine biodiversity during a time when Earth's biotic, climatic, and environmental systems underwent profound changes (Algeo et al., 2016). Sequence stratigraphic and paleontological analyses indicate the Bighorn Dolomite records the transition between greenhouse to icehouse conditions (Holland & Patzkowsky, 2012) prior to the start of the Hirnantian glaciation (Finnegan et al., 2011; Ghienne et al., 2014) and the late Ordovician mass extinction (Sepkoski, 1995; Sheehan, 2001). Thus, the Bighorn Dolomite serves as an important archive of events preceding significant global environmental and evolutionary change.

Of the four member subdivisions (Fig. 1), the Steamboat Point Member of the Bighorn Dolomite is the most persistent throughout Wyoming (Zenger, 1992). One of the defining features of the Steamboat Point Member is a centimeter- scale mottled fabric that resembles one found across Upper Ordovician strata from California to Newfoundland (Kendall, 1977; Jin et al., 2012). In the western Teton mountains, the basal Steamboat Point Member contains evidence for a microbial origin of the cm-scale mottled fabric (Bays et al., 2022), previously solely attributed to the action of burrowing organisms. Determining the origin and nature of mottled fabrics in upper Ordovician strata is significant for its use in paleoenvironmental or diagenetic reconstruction during this important transition in Earth history.

To determine the potential lateral extent and environmental significance of the microbial facies of the Bighorn Dolomite, I investigate the mottled fabrics of the Steamboat Point Member of the Bighorn Dolomite from Sheridan County, WY by analyzing Core C520 (44°55'47.2"N 106°13'26.4"W) which is housed in the United States Geological Survey (USGS) Core Research Center in Denver, CO. I investigate facies changes of the Steamboat Point Member and use texturally-resolved stable isotope and trace metal geochemistry to understand the nature of the facies changes, or alternatively, the extent of diagenesis. Furthermore, I compare these results to other regional sections to determine changes in depositional environments and discuss sea-level fluctuations and their relationship to redox conditions during deposition of the Steamboat Point Member.

Geologic Background

The Bighorn Dolomite of Wyoming was deposited over a 4–5-million- year interval (446 –450 Ma) during the Katian, the penultimate stage of the Ordovician (Blackwelder, 1913; Zenger, 1992; Holland & Patzkowsky, 2012). The dolostone was deposited at low latitudes in an open marine inner shelf environment (Fig. 2), when the North American Craton was equatorial (Lochman-Balk, 1971; Zenger ,1996; Holland & Patzkowsky, 2009). Transitions between biofacies that characterize the Bighorn Dolomite (e.g., brachiopod, gastropod, crinoid, dasyclad, and coral) have been well-established in the Bighorn Mountains of northern Wyoming (Holland & Patzkowsky, 2009; Patzkowsky & Holland, 2016).

The Bighorn Dolomite unconformably overlies the carbonate-rich Gallatin Formation of the upper Cambrian marine transgression (Lynds et al., 2010; Lochman & Hu, 1960). Above the unconformity that caps the Bighorn Dolomite lies the Upper Devonian–Upper Mississippian dolostones and limestones of the Darby and Jefferson Formations (Lynds et al., 2010; Becker & Lynds, 2012).

The Bighorn Dolomite is divided into four members (Fig. 1), the sequence architecture of which is interpreted to reflect deposition during a shift from low amplitude (~ 20 kyr) cyclicity to long period (100 kyr) cyclicity, indicating a shift from greenhouse conditions to icehouse conditions (Holland & Patzkowsky, 2012). The four members are the Lander Sandstone Member, the Steamboat Point Member, the Leigh Member, and the Horseshoe Mountain Member (Fig. 1). The lowermost member of the Bighorn Dolomite is the Lander Sandstone, a thin-bedded, carbonate-cemented quartz arenite (Miller, 1936). Forming cliffs above the Lander Sandstone is the massive, resistant dolostone of the Steamboat Point Member (Gierlowski & Langenheim, 1985). A fine-grained, laminated dolostone called the Leigh Member tops the unconformity above the Steamboat Point Member and transitions into an uppermost, clay-rich, highly fossiliferous dolomite known as the Horseshoe Mountain Member (Zenger, 1992). The Steamboat Point Member of western to central Wyoming (Lynds et al., 2010), of which this study is primarily concerned, consists of a deepening-upward transgressive systems tract in the bottom and a shallowing-upward highstand systems tract at the top (Holland & Patzkowsky, 2009).

Methods

Sample Collection

I observed, photographed, and sampled core C520 at the USGS Core Research Center in Denver, CO. Core C520 was selected because it contains the entire Steamboat Point Member of the Bighorn Dolomite. C520 was extracted from the region northeast of the Bighorn Mountains (44°55'47.2"N 106°13'26.4"W; see Figs. 2-3). The top of core C520 was at a depth of 3,178.2 m and the bottom was at 3,723.3 m. High-resolution photos were taken of the entire core and textural observations were recorded. Fourteen samples were collected at irregular intervals throughout the Steamboat Point Member for petrographic and geochemical analyses. Samples were also collected from the Teton Mountains (see Fig. 2) as discussed in Bays et al. (2022).

Petrographic Analyses

Samples of core C520 and from the exposure in the Teton Mounatins were cut, polished, and scanned on a flatbed scanner for high-resolution textural observations. Thin sections were prepared at varying thicknesses (~30 to 80 µm) for differential optical properties when viewed under the microscope. Thin sections were observed under transmitted, reflected, and cross polarized light on a Zeiss Axio Imager microscope and photomicrographs were created using Zen Software.

Geochemical Analyses

Fourteen sections of core C520 were powdered using a mill drill at SFSU for geochemical analysis. Each of the 14 targeted sections yielded a sample from both the light and dark mottled fabrics (Fig. 4), totaling 28 samples. Depths of the samples ranged from 3,546 m to 3,629.8 m below the surface. Ten samples of light and dark-textured powder were taken from 5 hand-samples that came from exposures in the Teton Mountains, also for geochemical analysis. The powdered samples averaged between 1.0 and 1.2 grams and were shipped to Washington State University for geochemical analysis.

All 38 samples were analyzed for $\delta^{18}O$, $\delta^{13}C$, according to standard procedure. Delta values were calculated using a three-point normalization from pure CO_2 evolved by phosphoric acid digestion of international carbonate references at 25°C. All samples were analyzed for iron, manganese, and strontium, in parts per million (ppm). Fourteen of the samples were analyzed for strontium isotopes: $^{86}Sr/^{88}Sr$, $^{87}Sr/^{86}Sr$, and $^{84}Sr/^{86}Sr$. Standard deviations were calculated for all analyses.

Scanning Electron Microscopy

Samples of core C520 were taken to the Electron Microscopy Lab at SFSU for imaging, and Energy dispersive X-ray spectroscopy (EDS) was used to identify and quantify elemental compositions. A specimen of core C520 from the reddish facies (Fig. 4) originating at 3,600 m depth was mounted on a standard petrographic slide and coated with 79 nm carbon using a Cressington 208-C high-vacuum evaporator (Ted Pella). The specimen was stored in a vacuum chamber prior to imaging to facilitate outgassing prior to introduction into the electron microscope sample chamber. Electron microscopy was performed using a Carl Zeiss ULTRA55 Field Emission Scanning Electron Microscope (FE- SEM) operating with a sample chamber vacuum below 3310-7 Torr. Electron micrographs were recorded with Everhart-Thornley (E-T) and Angle-Selective Backscattered detectors using an accelerating voltage of 10 keV, a working distance of 8.5 mm and a 120 μm diameter aperture operating in high-current mode. Energy Dispersive X-ray Spectrometry (EDS) was performed under the above FE-SEM operating conditions using an Oxford Instruments X-Max80 detector. The light and dark colored mottled textures were targeted separately in the analyses.

Results

Facies Observations

The Steamboat Point Member of the Bighorn Dolomite is composed of four distinct facies (Fig. 4). The bottom of the Steamboat Point Member, which lays above the Lander Sandstone, is a reddish color for approximately 9 m (Fig. 4). The reddish facies is composed of cm-scale mottled patterns, which Bays et al. (2022) interpreted as microbial thrombolite structures. The structures are deeper red, and the surrounding matrix is a lighter pink (Fig. 4A). On top of the reddish facies, the Steamboat Point Member becomes brownish for about 20 m. The mottled structures within the brownish facies are the same size and shape as within the underlying reddish facies (Fig. 4B). The structures in the brownish facies are a deeper shade of brown and the surrounding matrix is a lighter brown. Atop the brownish facies, microburrows (mm-scale diameter) are introduced into the Steamboat Point Member (Fig. 4C). For 30 m above the brownish facies, the facies is brownish with microburrows. Microburrows have a density of several per square decimeter on cut faces of Core C520. The color, size, and shape of the structures and matrix with the burrowed-brownish facies are the same as the underlying brownish facies. Above the burrowed-brownish facies, the facies becomes a burrowed-greyish for the upper 9 m of the Steamboat Point Member (Fig. 4D). The burrowed-greyish facies retains the same size, shape, and prevalence of structures and microburrows as the underlying burrowed-brownish facies.

For the entirety of the Steamboat Point Member, the mottled structures are a darker shade of color than the surrounding matrix. Dual geochemical measurements were performed on both the light and dark fabrics for every geochemical parameter listed in the Methods section, at every given depth of measurement on Core C520. No statistical difference was detected between structures and the matrix for any parameter.

Geochemical Measurements

Stable Isotopes

Stable isotopic carbon isotope values of dolomite have a mean value is -0.45 ‰ and a median of -0.32 ‰ (Table 1). The lowest $\delta^{13}C$ value is -1.63 ‰ and the highest is 0.48 ‰, with a range of 2.11 ‰. The standard deviation is 0.52. Carbon isotopes become heavier from the base of the Steamboat Point Member recording a positive shift that reaches its highest value at approximately 30 m above the base of the Steamboat Point Member (Fig. 5). For $\delta^{18}O$, the mean value is -6.09 ‰ and the median is also -6.09 ‰. The lowest value is -7.52 ‰ and the highest is -3.43 ‰, with a range of 4.09 ‰. The standard deviation is 0.74 (Table 1; Fig. 6).

Trace elements

Trace element concentrations were measured for Fe, Mn, and Sr (Table 2). The mean value for Fe is 4,747.68 ppm and the median is 2,146.0 ppm. The lowest value for Fe is 18.00 ppm and the highest is 46,093.00 ppm, with a range of 46,075 ppm. The standard deviation for Fe is 10,148.8 ppm. The greatest Fe concentrations occur at the base of the Steamboat Point Member and decline towards the top of the section (Fig. 7). For Mn, the mean value is 215.6 pmm and the median is 223.5 ppm. The lowest value is 7.0 ppm and the highest is 903.0 ppm, with a range of 896.0 ppm (Fig. 8). The standard deviation for Mn is 200.7 ppm. For Sr, the mean value is 52.1 ppm and the median is 32.7 ppm. The lowest value is 0.10 ppm and the highest is 453.7 ppm, with a range of 453.6 ppm (Fig. 9). The standard deviation for Sr is 70.7 ppm.

I measured three different ratios of Sr isotopes (^{87}Sr/^{86}Sr, ^{84}Sr/^{86}Sr, ^{86}Sr/^{88}Sr) on 14 samples (Table 3). For ^{87}Sr/^{86}Sr, the mean value is 0.709009 and the median is 0.7090515 (Fig. 10). The lowest value is 0.708438 and the highest is 0.709697, with a range of 0.001259. The standard deviation is 0.000339. For ^{84}Sr/^{86}Sr, the mean value is 0.0564947 and the median is 0.0564995. The lowest value is 0.056460 and the highest is 0.0565150, with a range of 0.000055. The standard deviation is 0.0000163. For ^{86}Sr/^{88}Sr, the mean value is 0.114411 and the median is 0.114416. The lowest value is 0.114349 and the highest is 0.114472, with a range of 0.000123. The standard deviation is 0.0000440.

Scanning Electron Microscopy

In SEM imaging, we detected micropores on the scale of tens-to-hundreds of μm for a sample of the reddish mottled facies at 3,600 m depth (Figs. 11-13). We also detected abundant dark, smooth patches on the scale of hundreds of μm in diameter. We performed EDS analysis on the dark patches, as well as the surrounding, proximal dolomite crystals, to determine elemental percentages (Fig. 12).

Energy Dispersive Spectroscopy

I conducted EDS analysis (C, O, Mg, Ca) 25 times on dolomite crystals next to a dark patch. All values are in atomic %. For C, the mean value is 78.46. The lowest value is 45.86 and the highest is 96.90. The standard deviation is 14.41. For O, the mean value is 11.35. The lowest value is 0.00 and the highest is 25.91. The standard deviation is 6.75. For Mg, the mean value is

5.07. The lowest value is 0.21 and the highest is 22.29. The standard deviation is 5.79. For Ca, the mean value is 5.12. The lowest value is 0.00 and the highest is 35.18. The standard deviation is 9.46 (Fig. 12).

I conducted EDS analysis (C, O, F, Cl) 25 times on a dark patch adjacent to the dolomite measurements (Tables 4-5). All values are in atomic %. For C, the mean value is 91.13. The lowest value is 83.09 and the highest is 98.60. The standard deviation is 3.55. For O, the mean value is 8.33. The lowest value is 0.86 and the highest is 16.37. The standard deviation is 3.50. For F, the mean value is 0.39. The lowest value is 0.09 and the highest is 0.69. The standard deviation is 0.14. For Cl, the mean value is 0.16. The lowest value is 0.00 and the highest is 0.69. The standard deviation is 0.14.

Discussion

Facies in the Steamboat Point Member of the Bighorn Dolomite pass through four distinct phases. The basal Lander Sandstone that underlies the Steamboat Point Member is a thin transgressive sandstone that is typically poorly exposed throughout Wyoming (Holland & Patzkowsky, 2009). Most of the Steamboat Point Member consists of open shallow subtidal facies with inner shallow subtidal deposits near its top. Overlaying the Steamboat Point Member, the Leigh Member is composed entirely of inner shallow subtidal to peritidal flat deposits (Holland & Patzkowsky, 2009).

Holland & Patzkowsky (2009; 2012) delineated three sections to the Steamboat Point Member: the bottom half, which conformably begins after the Lander Sandstone, is a deepening-upward, inner tidal facies; the middle of the Steamboat Point Member is a highstand facies lasting several meters; the top half of the Steamboat Point Member is a shallowing-upward facies, culminating with the peritidal Leigh Member. The data presented in this thesis is interpreted with the aforementioned sequence stratigraphic framework for reference.

Fig. 4 shows the four distinct facies in the Steamboat Point Member, as shown in Core C520 (USGS Core Research Center). From bottom to top: Reddish facies (approximately 9 m) Brownish facies (approximately 20 m); Brownish facies with microburrows (approximately 30 m.); Greyish facies with microburrows (approximately 9 m).

The behavior of trace elements, carbon isotopes, and facies changes indicates a dynamic story of ocean circulation (Figs. 14-15). Table 2 shows the behavior of trace elements. The concentration of iron in the Steamboat Point Member, from the Lander Member to the Leigh Member, as shown in Core C520 in Figure 14, went from high (average over 45,000 ppm) to low (average under 2,000 ppm). During this same interval, manganese also went from high (average over 800 ppm) to low (an average of approximately 250 ppm; Fig. 14). Carbon isotopes experienced a concurrent positive excursion of 2.0 per mil (-1.5 per mil at the lowest to +0.5 per mil at the highest) (Fig. 5 & Fig. 14). All geochemical data is associated with a particular facies depiction (Figure 4; 14).

Trace elements and facies interpretations

During deposition of the Lander Sandstone, sea level was low (Holland & Patzkowsky, 2009; 2012) and the depositional environment was peritidal and inner tidal (bottom of Fig. 15). With rising sea level, deposition of the Steamboat Point Member dolomite took place (Holland & Patzkowsky, 2009; 2012). During initial deposition of the Bighorn Dolomite, while sea level was low, the Laurentian Sea remained relatively isolated from the open ocean (Pratt & Holmden, 2008; Wetzel et al., 2013). Moreover, the section of the Laurentian Sea representing the depositional environment of the Bighorn Dolomite had varying degrees of connection with other depositional environments within the Sea of Laurentia (Wetzel et al., 2013).

In that relatively isolated state following deposition of the Lander Sandstone, the depositional environment of the Bighorn Dolomite had high iron and manganese concentrations (Fig. 14), which may have come from felsic weathering nearby (Panchuk et al., 2005), and/or been influenced by oxygen levels in the water (Tribovillard et al., 2006; Freeman et al., 2004). Iron and manganese, being redox-sensitive trace metals, bond strongly with oxygen; the metals do not incorporate into the carbonate crystal lattice in an oxidized state (James & Jones, 2016; Scholz et al., 2011). The lower Steamboat Point Member contains high trace metal concentrations (Fig. 14), which is reflected in the reddish color characteristic of oxidized iron (Fig. 4A; O'Connell et al., 2020).

As sea level continued to rise, the depositional waters of the Steamboat Point Member of the Bighorn Dolomite became connected with other sections of the epeiric sea and eventually the open ocean (Allison & Wells, 2006; Wetzel et al., 2013). As waters experienced transfer with the open ocean, the trace metal concentrations reduced and equilibrated with the open ocean (Holmden et al., 1998; Panchuk et al., 2005). As the iron and manganese concentration decreased (Fig. 14), the color of the facies likewise became less reddish and more brownish (O'Connell et al., 2020; Fig. 4B).

At the sea level highstand that occurred in the middle of the Steamboat Point Member (Holland & Patzkowsky, 2009; 2012), waters experienced maximum circulation and mixing with the open ocean (Allison & Wells, 2006). The enhanced circulation with other regions of

Laurentia and the open ocean allowed burrowing organisms to migrate into the depositional environment of the Bighorn Dolomite (Lam & Stigall, 2015; Nawrot et al., 2015; Biton, 2020). The Steamboat Point Member facies, as demonstrated in Core C520, remained brownish and acquired small microburrows in the middle of the section, consistent with both Holland and Patzkowsky's (2009; 2012) description of sea level behavior and Biton's (2020) characterization of species migration at high sea level (Fig. 4C).

As sea level regressed, the depositional environment of the Bighorn Dolomite became relatively disconnected from the open ocean and other regions of the Laurentian Sea (Holland & Patzkowsky, 2009; 2012; Allison & Wells, 2006; Wetzel et al., 2013). In the upper Steamboat Point Member, which occurred perhaps 1-2 million years after the end of the Lander Sandstone (Becker & Lynds, 2012; Holland & Patzkowsky, 2012), the conditions that engendered high iron/manganese deposition early on had become comparable with the open ocean (i.e., lower levels of trace metals). As sea level dropped, the burrowing organisms that arrived during high sea level remained in the Bighorn Dolomite depositional environment (Nawrot et al., 2015). Trace metal concentrations likewise remained low in the upper Steamboat Point Member (Fig. 14). The facies became greyish and retained the small burrows that had appeared during sea level highstand (Fig. 4D). After the upper section of the Steamboat Point Member, the depositional environment of the Bighorn Dolomite continued to shallow, becoming the peritidal and inner tidal facies of the Leigh Member (Holland & Patzkowsky, 2009; 2012). This is corroborated by the author's visual observations of evaporites in the uppermost part of the Steamboat Point Member underlying the Leigh Member.

Carbon isotope excursion, chemostratigraphy, and facies interpretations

Chemostratigraphy has the potential to allow for correlation of Late Ordovician sequences at the local, regional, and global level (Bergström et al., 2010; Bergström et al., 2015; Jing, et al., 2019). Several prominent intercontinental $\delta^{13}C$ excursions have been identified in Late Ordovician strata (Figs. 16-17; Bergström et al., 2010; Jing, et al., 2019). The two most recognizable Late Ordovician excursions are the early Katian Guttenberg carbon isotope excursion (GICE) and the Hirnantian carbon isotope excursion (HICE) (Brookfield & Hannigan, 2021; Bergström et al., 2010; 2015). Several subdominant excursions have also been correlated, from Laurentia to Baltoscandia (Bergström et al., 2010; Jing et al., 2019; Brookfield & Hannigan, 2021). Carbon isotope chemostratigraphy may be used for high-resolution correlation due to increasing acceptance of its inherent synchroneity across marine geographies (Bergström et al., 2010; Bergström et al., 2015; Jing, et al., 2019; Fanton & Holmden, 2007).

Plotting $\delta^{13}C$ as a function of depth within the Bighorn Dolomite core reveals a $\delta^{13}C$ excursion (Figs. 5; 14). The lowest measured depth, which corresponds to the dolomite deposited above the Lander Sandstone, is relatively enriched in ^{12}C and depleted in ^{13}C (Figs. 5; 14). The $\delta^{13}C$ increases to its highest value in the middle of the Steamboat Point Member, representing the apex of the excursion (Figs. 5; 14). The top half of the Steamboat Point is characterized by a gradual decrease in $\delta^{13}C$ until the facies becomes the Leigh Member tidal flat facies (Figs. 5; 14).

The $\delta^{13}C$ excursion detected in the Steamboat Point Member is likely the Fairview Excursion (Figs. 16-17; Jing et al., 2019; Bergström et al., 2010; Bergström et al., 2015), based on the C2 conodont zone (Oulodus *velicuspis* to Oulodus *robustus*) attributed to the Steamboat Point Member of the Bighorn Dolomite (Holland & Patzkowsky, 2009; Amsden & Miller, 1942;

Stone & Furnish, 1959; Sweet, 1979; 1984). The Fairview Excursion has also been corelated with carbonate rocks in Central China, Baltoscandia, and the Cincinnati region of the United States (Figs. 16-17; Bergström et al., 2010; 2015; Jing et al., 2019).

As shown in Figure 15, carbon isotopes and sea level are likely corelated by a causal relationship (Fanton & Holmden, 2007). On the basis of Katian rocks from Iowa, Fanton & Holmden (2007) concluded the $\delta^{13}C$ excursions were directly associated with sea level flooding events due to circulation patterns.

In modern carbonate depositional environments, $\delta^{13}C$ values are up to 4‰ lower than the open ocean (Fanton & Holmden, 2007; Lloyd 1964; Patterson & Walter, 1994). Higher ^{12}C is associated with nearshore environments, and higher ^{13}C is concentrated in deeper water (Fanton & Holmden, 2007; Kolata et al., 2001; Fanton et al., 2002). Much like the Florida Bay and the Bahamas Banks, the epeiric seas of the Paleozoic may have overprinted this fractionation effect (Fanton & Holmden, 2007; Kolata et al., 2001; Ludvigson et al., 2004).

The process controlling the carbon isotope distribution on seafloor deposition is outlined by Fanton & Holmden (2007) and shown in (Fig. 15). As the sea level rises, so does the pycnocline, relative to the place of deposition (Woods, 1985; Fig.15). In equatorial areas, the pycnocline follows the thermocline: the hotter the water, the higher the thermocline (Woods, 1985; Gnanadesikan, 1999). The Late Ordovician was a greenhouse climate, and the Sea of Laurentia, being equatorial (Torsvik et al., 1995; Jin et al., 2013; Becker & Lynds, 2012), had a pycnocline relatively close to the water surface (Woods, 1985; Gnanadesikan, 1999). The rising sea level and pycnocline draws eutrophic waters, which travel along the seafloor, towards higher elevations on the ramp or bank (Fig. 15; Fanton & Holmden, 2007). As the eutrophic waters move higher on the area of carbonate deposition, higher proportions of ^{13}C are deposited below the pycnocline, where the abrupt change in density occurs (Fig. 15; Woods, 1985; Gnanadesikan, 1999; Fanton & Holmden, 2007).

Above the pycnocline, higher proportions of ^{12}C are deposited in the carbonate rocks (Fig. 15; Patterson & Walter, 1994; Lloyd, 1964; Fanton & Holmden, 2007). The eutrophic waters that circulate below the pycnocline are rich in nutrients, leading to rampant decomposition resulting in anoxia of bottom waters (Fig. 15; Anderson et al., 2002; Fanton & Holmden, 2007). Therefore, at low sea level, the Steamboat Point Member has a relatively higher proportion of ^{12}C; at high sea level, the pycnocline moves to higher elevation on the ramp or bank, bringing a higher proportion of the heavier carbon isotope (^{13}C) to the depositional environment of the Bighorn Dolomite (Fig. 15; Woods, 1985; Gnanadesikan, 1999; Patterson & Walter, 1994; Lloyd, 1964; Fanton & Holmden, 2007).

Anoxia of depositional waters affects the concentration of trace metals (Scholz et al., 2011), and the highest concentrations of trace metals in the Bighorn Dolomite occur at the basal portion of the Steamboat Point (Fig. 7). The trajectory of the trace metal data indicates the possibility of an overall decrease in anoxia in the epeiric sea, coinciding with the arrival of burrowing organisms (Fig. 4). Burrowing of sediments induces downward transport of oxygen into the substrate, decreasing anoxia (Kristensen, 2000).

The $\delta^{13}C$ excursion can be precisely correlated to other carbonate units, both regionally and globally, because sea level is controlled by global (eustatic) and local (uplift/subsidence), processes (Peeters et al., 1998; Fanton & Holmden, 2007; Răbăgia et al., 2011). Figures 16-17 show the Fairview excursion (C2 conodont zone in North America) in the Cincinnati region, central China, Oklahoma, Iowa, and dampened in Estonia (Bergström et al., 2010; Bergström et al., 2015; Fanton & Holmden, 2007). Facies descriptions match sea level forcing for units in the Midcontinent region, while others, especially internationally, may be out of phase (Jing et al., 2019; Fanton & Holmden, 2007), due to differences in lithostatic flexure, proximity to shoreline, or resolution (Young et al., 2005; Fanton & Holmden, 2007; Peeters et al., 1998). Many researchers dispute the link between sea level and carbon isotope excursion; however, the correlative power of the carbon excursions is widely accepted (Bergström et al., 2010; 2015; Jing et al., 2019; Fanton & Holmden, 2007; Brookfield & Hannigan, 2021).

Given the large number of carbonates across the Laurentian basin that are coeval with the Bighorn Dolomite, future investigations of carbon isotope chemostratigraphy and facies matching may yield high-precision correlations. Coeval Laurentian rocks include the Red River Formation and Stony Mountain Formations of Manitoba (Elias, 1991), the Fremont Dolomite of Colorado (Holland & Patzkowsky, 2012), the Fish Haven and Ely Springs Dolomites of Nevada and Utah (Harris & Sheehan, 1996), and the Aleman, Cutter, and Upham Formations of the Montoya Group of New Mexico and west Texas (Pope, 2004).

Diagenesis

It is important to assess how much diagenesis may have occurred when interpreting the geochemistry. One indicator of diagenesis is the correlation between $\delta^{13}C$ and $\delta^{18}O$, which occurs because of interactions between pore water and rock (Algeo et al., 1992). A cross plot (Fig. 19) of $\delta^{13}C$ and $\delta^{18}O$ shows no correlation, indicating no significant replacement of ions from pore water (Algeo et al., 1992).

Figure 18 shows oxygen isotope values for the Paleozoic (Goldberg et al. 2021), and Fig. 6 shows the values obtained in this study. Mean and median $\delta^{18}O$ in the Bighorn Dolomite both equal -6.09 per mil (VPDB), which is close to the global average (Goldberg et al., 2021). This synchroneity supports the assumption that oxygen has not undergone significant diagenesis, having retained depositional values (Zenger, 1996).

Further evidence for lack of extensive diagenesis includes well-preserved fossils, low conodont color indices, and fine crystallinity (Zenger 1992; 1996). Under the microscope, the sedimentary structures in the Bighorn Dolomite retain primary characteristics, indicating a dearth in diagenesis (Bays et al., 2022; Zenger, 1992; 1996). In a previous study, we observed thrombolitic laminations in thin section, which appear to be preserved from deposition (Bays et al., 2022). The crystals within the thrombolitic structures are relatively small and lack any visible cementation (Fig. 13), which suggests formation in open, carbonate supersaturated water (Meister et al., 2011; Bays et al., 2022). Underground diagenetic dolomitization would likely obfuscate such fabrics (James & Jones, 2016).

Thus, analyses of stable isotopes and petrography indicate the dolomite crystals likely preserve the carbon and oxygen signatures of deposition. Stable isotopes are likely preserved in the Steamboat Point Member of the Bighorn Dolomite; however, diagenesis is unavoidable to a certain extent (Land, 1983; Jing et al., 2019).

A cross plot of Sr ppm and $^{87}Sr/^{86}Sr$ reveals a conspicuous linear array (Fig. 20). Such a relationship between Sr ppm and $^{87}Sr/^{86}Sr$ indicates diagenesis occurred with strontium which is expected from this bulk rock analysis (Banner, 1995; Gao, 1990). For that reason, Sr concentration and isotopic data is considered unusable as a proxy for depositional conditions.

SEM/ EDS Analysis

SEM images of Core C520 reveal different micrometer-scale fabrics (Fig. 11), and energy-dispersive X-ray spectroscopy (EDS) performed on the two fabrics (light and dark) revealed them to have different elemental compositions (Tables 4, 5). The dolomite crystals are 78% carbon, 11% oxygen, and 5% magnesium, allowing us to confirm dolomite composition ($CaMg(CO_3)_2$) (James & Jones, 2016). The dark patches are 91% carbon and 8% oxygen, which, when combined with SEM observations, leads us to conclude they are patches of hydrocarbons (Olah et al., 2018). The Red River Formation of Manitoba, a coeval unit whose mottled fabric resembles the Bighorn Dolomite, is an important petroleum reserve (Kendall, 1984; Clement, 1985).

Figure 12 shows the hydrocarbons to be located near nanopores and micropores in the sediment matrix of the dolomite. The hydrocarbons are not common in the microbial structures (Fig. 12). Dolomite-related nano/micropores form in three ways (Nesheim et al., 2016): (1) "overdolomitization," (2) contrasting precipitation/replacement processes, and (3) transformation of Mg-calcite to microrhombic calcite and later dolomitization (Nesheim et al., 2016). It is likely that contrasting precipitation and replacement processes are the cause for the nano- and micropores in the Bighorn Dolomite, due to evidence for primary precipitation. Megapores are not common in the Bighorn Dolomite, and permeability is negligeable (Blackwelder, 1913); the pores are neither big enough nor prevalent enough for significant flow rates of the hydrocarbon reserves (Nesheim et al., 2016).

Conclusion

The Bighorn Dolomite of Wyoming and adjacent states is an upper Ordovician dolostone deposited prior to the end Ordovician glaciation and mass extinction. The fabric of the Steamboat Point Member of the Bighorn Dolomite contains microbialite textures similar to coeval dolostones from the Laurentian Sea basin. We analyzed textures and tested stable isotopes (carbon, oxygen), trace elements (iron, manganese, strontium), and strontium isotopes. We also used SEM imaging to detail micrometer-scale features. Geochemical interpretation, in tandem with facies observations, tells a story of sea level transgression and regression. A carbon isotope excursion was detected and correlated, from conodont data, with the Katian Fairview excursion. Trace element concentrations and burrow stratigraphy, in light of concurrent sea level excursion, suggest eustasy as their primary driver. Diagenesis likely occurred with respect to strontium, however oxygen and carbon are interpreted as likely depositional. The preponderance of evidence indicates the depositional environment of the Steamboat Point Member experienced the rise and fall of a sea level excursion that predated the major climate oscillation of the end Ordovician.

References

Algeo, T. J., Marenco, P. J., & Saltzman, M. R. (2016). Co-evolution of oceans, climate, and the biosphere during the 'Ordovician Revolution': A Review. *Palaeogeography, Palaeoclimatology, Palaeoecology*, *458*, 1–11. https://doi.org/10.1016/j.palaeo.2016.05.015

Algeo, T., Lohmann, K., & Wilkinson, B. (1992). Meteoric-burial diagenesis of Middle Pennsylvanian limestones in the Orogrande Basin, New Mexico: Water/rock interactions and basin Geothermics. *SEPM Journal of Sedimentary Research*, *Vol. 62*. https://doi.org/10.1306/d426797e-2b26-11d7-8648000102c1865d

Allison, P. A., & Wells, M. R. (2006). Circulation in large ancient Epicontinental Seas: What was different and why? *PALAIOS*, *21*(6), 513–515. https://doi.org/10.2110/palo.2006.s06

Amsden, T. W., & Miller. (1942). *Ordovician conodonts from the Bighorn Mountains of Wyoming*. Journal of Paleontology.

Anderson, D. M., Glibert, P. M., & Burkholder, J. M. (2002). Harmful algal blooms and eutrophication: Nutrient sources, composition, and consequences. *Estuaries*, *25*(4), 704–726. https://doi.org/10.1007/bf02804901

Banner, J. (1995). Application of the trace element and isotope geochemistry of strontium to studies of carbonate diagenesis. *Sedimentology*, *42*(5), 805–824. https://doi.org/10.1111/j.1365-3091.1995.tb00410.x

Bays, A. Ibarra, Y., Sanon, S., and Hayzelden, C. (2022). Taphonomic controls on microbialite textures from the steamboat point member, Upper Ordovician Bighorn Dolomite, Western Teton Mountains, USA. *PALAIOS*, *37*(5), 150–164. https://doi.org/10.2110/palo.2021.042

Becker, T.P. and Lynds, R., (2012), A geologic deconstruction of one of the world's largest natural accumulations of CO2, Moxa arch,southwestern Wyoming: American Associ- ation of Petroleum Geologists Bulletin, v. 96, p. 1643–1664, doi: 10.1306/01251211089.

Biton, E. (2020). Possible implications of sea level changes for species migration through the Suez Canal. *Scientific Reports*, *10*(1). https://doi.org/10.1038/s41598-020-78313-2

Blackwelder, E., (1913), Origin of the Bighorn Dolomite of Wyoming: Bulletin of the Geological Society of America, v. 24, p. 607–624.

Blakey paleogeographic maps. Geology and Environmental Geosciences. (2013), from https://geology.lafayette.edu/2022/09/02/blakey-paleogeographic-maps/

Bergström, S. M., Saltzman, M. R., Leslie, S. A., Ferretti, A., & Young, S. A. (2015). Trans-Atlantic application of the Baltic Middle and Upper Ordovician carbon isotope zonation. *Estonian Journal of Earth Sciences*, *64*(1), 8. https://doi.org/10.3176/earth.2015.02

Bergström, S. M., Young, S., & Schmitz, B. (2010). Katian (Upper Ordovician) Δ13C chemostratigraphy and sequence stratigraphy in the United States and Baltoscandia: A regional comparison. *Palaeogeography, Palaeoclimatology, Palaeoecology*, *296*(3-4), 217–234. https://doi.org/10.1016/j.palaeo.2010.02.03

Brookfield, M. E., & Hannigan, R. E. (2021). Carbon and oxygen isotope variations in Shell Beds from the upper ordovician (mid-cincinnatian: Maysvillian to early Richmondian) of ontario: Evaluation of the warm saline deep ocean hypothesis, paleoceanographic changes, and Milankovitch orbital cycles in the transition to the Hirnantian glaciation. *Palaeogeography, Palaeoclimatology, Palaeoecology*, *577*, 110528. https://doi.org/10.1016/j.palaeo.2021.110528

Clement, J. H. (1985). Depositional sequences and characteristics of Ordovician Red River Reservoirs, Pennel Field, Williston Basin, Montana. *Casebooks in Earth Sciences*, 71–84. https://doi.org/10.1007/978-1-4612-5040-1_5

Elias, R.J., (1991), Environmental cycles and bioevents in the Upper Ordovician Red River–Stony Mountain solitary rugose coral province of North America, *in* Barnes, C.R., and Williams, S.H., eds., Advances in Ordovician Geology: Geological Sur- vey of Canada Paper 90-9, Geological Survey of Canada, Ottawa, p. 205–211.

Fanton, K.C., Holmden, C., Nowlan, G.S., and Haidl, F.M. 2002. 143Nd/144Nd and Sm/Nd stratigraphy of Upper Ordovician epeiric sea carbonates. Geochimica et Cosmochimica Acta, **66**: 241–255.

Fanton, K. C., & Holmden, C. (2007). Sea-level forcing of carbon isotope excursions in Epeiric Seas: Implications for chemostratigraphy. *Canadian Journal of Earth Sciences*, *44*(6), 807–818. https://doi.org/10.1139/e06-122

Finnegan, S., Bergmann, K., Eiler, J.M., Jones, D.S., Fike, D.A., Eisenman, I., Hughes, N.C., Tripati, A.K., and Fischer, W.W., 2011, The magnitude and duration of Late Ordovician–early Silurian glaciation: Science, v. 331, p. 903–906, doi: 10.1126/science.1 200803.

Fortey, R. A., & Cocks, L. R. (2005). Late Ordovician global warming—the Boda Event. *Geology*, *33*(5), 405. https://doi.org/10.1130/g21180.1

Freeman, C., Fenner, N., Ostle, N. J., Kang, H., Dowrick, D. J., Reynolds, B., Lock, M. A., Sleep, D., Hughes, S., & Hudson, J. (2004). Export of dissolved organic carbon from peatlands under elevated carbon dioxide levels. *Nature*, *430*(6996), 195–198. https://doi.org/10.1038/nature02707

Gao, G. (1990). Geochemical and isotopic constraints on the diagenetic history of a massive stratal, late cambrian (royer) dolomite, Lower Arbuckle Group, Slick Hills, SW Oklahoma, USA. *Geochimica Et Cosmochimica Acta*, *54*(7), 1979–1989. https://doi.org/10.1016/0016-7037(90)90266-n

Ghienne, J.F., Desrochers, A., Vandenbroucke, T.R.A., Achab, A., Asselina, E., Dabard, M.P., Farley, C., Loi, A., Paris, F., Wickson, S., and Veizer, J., 2014, A Cenozoic-style scenario for the end-ordovician glaciation: Nature Communications, v. 5, doi: 10.1038/ ncomms5485.

Gierlowski, T.C. and Langenheim, R.L., 1985, Corals from the Late Ordovician Horseshoe Mountain Member, Bighorn Dolomite, Bighorn Mountains, Sheridan County, Wyoming: Earth Science Bulletin, v. 18, p. 1–21.

Gnanadesikan, A. (1999). A simple predictive model for the structure of the Oceanic Pycnocline. *Science*, *283*(5410), 2077–2079. https://doi.org/10.1126/science.283.5410.2077

Goldberg, S. L., Present, T. M., Finnegan, S., & Bergmann, K. D. (2021). A high-resolution record of early paleozoic climate. *Proceedings of the National Academy of Sciences*, *118*(6). https://doi.org/10.1073/pnas.2013083118

Harris, M.T., and Sheehan, P.M., 1996, Upper Ordovician–Lower Silurian depositional sequences determined from middle shelf sections, Barn Hills and Lakeside Mountains, eastern Great Basin, *in* Witzke, B.J., Ludvigson, G.A., and Day, J., eds., Paleozoic Sequence Stratigraphy: Views from the North American Craton: Geological Society of America Special Papers, v. 306, p. 161–176.

Holland, S. M., & Patzkowsky, M. E. (2009). The stratigraphic distribution of fossils in a tropical carbonate succession: Ordovician bighorn dolomite, Wyoming, USA. *PALAIOS*, *24*(5), 303–317. https://doi.org/10.2110/palo.2008.p08-095r

Holland, S.M. and Patzkowsky, M.E., 2012, Sequence architecture of the Bighorn Dolomite, Wyoming , USA: transition to the late Ordovician Icehouse: Journal of Sedimentary Research, v. 82, p. 599–615, doi: 10.2110/jsr.2012.52.

Holmden, C., Creaser, R.A., Muehlenbachs, K., Leslie, S.A., and Bergström, S.M. 1998. Isotopic evidence for geochemical de- coupling between ancient epeiric seas and bordering oceans: implications for secular curves. Geology, **26**: 567–570.

Horita, J. (2014). Oxygen and carbon isotope fractionation in the system dolomite–water–CO2 to elevated temperatures. *Geochimica Et Cosmochimica Acta*, *129*, 111–124. https://doi.org/10.1016/j.gca.2013.12.027

Husinec, A., & Harvey, L. A. (2021). Late Ordovician climate and sea-level record in a mixed carbonate-siliciclastic-evaporite lithofacies, Williston Basin, USA. *Palaeogeography, Palaeoclimatology, Palaeoecology*, *561*, 110054. https://doi.org/10.1016/j.palaeo.2020.110054

James, N. P., & Jones, B. (2016). *Origin of carbonate sedimentary rocks*. John Wiley & Sons, Inc.

Jin, J., Harper, D.A.T., Rasmussen, J.A., and Sheehan, P.M., 2012, Late Ordovician massive-bedded Thalassinoides ichnofacies along the palaeoequator of Laurentia: Palaeogeography, Palaeoclimatology, Palaeoecology, v. 367–368, p. 73–88, doi: 10.1016/ j.palaeo.2011.05.023.

Jin, J., Harper, D. A., Cocks, L. R., McCausland, P. J., Rasmussen, C. M., & Sheehan, P. M. (2013). Precisely locating the Ordovician equator in Laurentia. *Geology*, *41*(2), 107–110. https://doi.org/10.1130/g33688.1

Jing, X., Stouge, S., Tian, Y., Wang, X., & Zhou, H. (2019). Katian (Upper Ordovician) carbon isotope chemostratigraphy in the Neixiang area, Central China: Implications for intercontinental correlation. *Geological Magazine*, *156*(12), 2053–2066. https://doi.org/10.1017/s0016756819000372

Kendall, A.C., 1977, Origin of dolomite mottling in Ordovician limestones from Saskatchewan and Manitoba: Bulletin of Canadian Petroleum Geology, v. 25, p. 480– 504.

Kendall, A. (1984). Origin and geometry of Red River Dolomite Reservoirs, Western Williston Basin: Discussion. *AAPG Bulletin*, *68*. https://doi.org/10.1306/ad461390-16f7-11d7-8645000102c1865d

Kiipli, E., Kiipli, T., Kallaste, T., & Pajusaar, S. (2017). Trace elements indicating humid climatic events in the ordovician–early silurian. *Geochemistry*, *77*(4), 625–631. https://doi.org/10.1016/j.chemer.2017.05.002

Kolata, D.R., Huff, W.D., and Bergström, S.M. 2001. The Ordovician Sebree Trough: an oceanic passage to the Midcontinent United States. Geological Society of America Bulletin, **113**: 1067–1078.

Kristensen, E. (2000). Organic matter diagenesis at the oxic/anoxic interface in coastal marine sediments, with emphasis on the role of burrowing animals. *Life at Interfaces and Under Extreme Conditions*, 1–24. https://doi.org/10.1007/978-94-011-4148-2_1

Lam, A. R., & Stigall, A. L. (2015). Pathways and mechanisms of late ordovician (katian) faunal migrations of Laurentia and Baltica. *Estonian Journal of Earth Sciences*, *64*(1), 62. https://doi.org/10.3176/earth.2015.11

Lloyd, R. M. (1964). Variations in the oxygen and carbon isotope ratios of Florida Bay mollusks and their environmental significance. *The Journal of Geology*, *72*(1), 84–111. https://doi.org/10.1086/626966

Lochman, C. and Hu, C., 1960, Upper Cambrian Faunas from the Northwest Wind River Mountains, Wyoming. Part I: Journal of Paleontology, v. 34, p. 793–834.

Lochman-Balk, C., 1971, The Cambrian of the craton of the United States, in C.H. Holland (ed.), Cambrian of the New World: John Wiley and Sons, Inc, New York, p. 79– 167.

Ludvigson, G.A., Jacobsen, S.R., Witzke, B.J., and González, L. 1996. Carbonate component chemostratigraphy and depositional history of the Ordovician Decorah Formation, Upper Mississippi Valley. *In* Paleozoic sequence stratigraphy: views from the North American craton. *Edited by* B.J. Witzke, G.A. Ludvigson, and J. Day. The Geological Society of America, Special Paper 306, pp. 307–330.

Lynds, R., Campbell-Stone, E., Becker, T.P., and Frost, C.D., 2010, Stratigraphic evaluation of reservoir and seal in a natural CO2 field: lower Paleozoic, Moxa Arch, southwest Wyoming: Rocky Mountain Geology, v. 45, p. 113–132, doi: 10.2113/gsrocky. 45.2.113.

Meister, P., Reyes, C., Beaumont, W., Rincon, M., Collins, L., Berelson, W., Scott, L., Corsetti, F., & Nealson, K. (2011). Calcium and magnesium-limited dolomite precipitation at Deep Springs Lake, California. *Sedimentology*, *58*(7), 1810–1830. https://doi.org/10.1111/j.1365-3091.2011.01240.x

Miller, B.M., 1936, Cambrian stratigraphy of northwestern Wyoming: The Journal of Geology, v. 44, p. 113–144, doi: 10.1086/624413.

Nawrot, R., Chattopadhyay, D., & Zuschin, M. (2015). What guides invasion success? ecological correlates of arrival, establishment and spread of Red Sea bivalves in the Mediterranean Sea. *Diversity and Distributions*, *21*(9), 1075–1086. https://doi.org/10.1111/ddi.12348

Nesheim, T., LeFever, J., & Bader, J. (2016). *Red River Formation - Department of Mineral Resources, North Dakota*. 2016 Core Workshop. Retrieved December 3, 2022, from https://www.dmr.nd.gov/ndgs/documents/Publication_List/pdf/GEOINV/GI-196.pdf

O'Connell, B., Wallace, M. W., Hood, A. v.S., Lechte, M. A., & Planavsky, N. J. (2020). Iron-rich carbonate tidal deposits, Angepena Formation, South Australia: A redox-stratified cryogenian basin. *Precambrian Research*, *342*, 105668. https://doi.org/10.1016/j.precamres.2020.105668

Olah, G. A., Molnár Árpád, & Surya, P. G. K. (2018). *Hydrocarbon chemistry*. John Wiley & Sons, Inc.

Panchuk, K. M., Holmden, C., & Kump, L. R. (2005). Sensitivity of the epeiric sea carbon isotope record to local-scale carbon cycle processes: Tales from the Mohawkian Sea. *Palaeogeography, Palaeoclimatology, Palaeoecology*, *228*(3-4), 320–337. https://doi.org/10.1016/j.palaeo.2005.06.019

Patterson, W. P., & Walter, L. M. (1994). Depletion of 13C in seawater ΣC02 on modern carbonate platforms: Significance for the carbon isotopic record of carbonates. *Geology*, *22*(10), 885. https://doi.org/10.1130/0091-7613(1994)022<0885:docisc>2.3.co;2

Patzkowsky, M.E. and Holland, S.M., 2016, Biotic invasion, niche stability, and the assembly of regional biotas in deep time: comparison between faunal provinces: Paleobiology, v. 42, p. 359–379, doi: 10.1017/pab.2016.1.

Peeters, Hoek, Brinkhuis, Wilpshaar, de Boer, Krijgsman, & Meulenkamp. (1998). Differentiating Glacio-Eustacy and tectonics; a case study involving dinoflagellate cysts from the eocene-oligocene transition of the pindos foreland basin (NW greece). *Terra Nova*, *10*(5), 245–249. https://doi.org/10.1046/j.1365-3121.1998.00198.x

Pope, M.C., 2004, Cherty carbonate facies of the Montoya Group, southern New Mexico and western Texas and its regional correlatives: A record of Late Ordo- vician paleoceanography on southern Laurentia: Palaeogeography, Palaeoclima- tology, Palaeoecology, v. 210, p. 367–384.

Pratt, B. R., & Holmden, C. (2008). MODERN AND ANCIENT EPEIRIC SEAS AND THE SUPER-ESTUARINE CIRCULATION MODEL OF MARINE ANOXIA. In *Dynamics of epeiric seas*. essay, Geological Association of Canada.

Răbăgia, T., Matenco, L., & Cloetingh, S. (2011). The interplay between eustacy, tectonics and surface processes during the growth of a fault-related structure as derived from sequence stratigraphy: The govora–Ocnele Mari antiform, South Carpathians. *Tectonophysics*, *502*(1-2), 196–220. https://doi.org/10.1016/j.tecto.2009.09.017

Scholz, F., Hensen, C., Noffke, A., Rohde, A., Liebetrau, V., & Wallmann, K. (2011). Early diagenesis of redox-sensitive trace metals in the Peru upwelling area – response to ENSOrelated oxygen fluctuations in the water column. *Geochimica Et Cosmochimica Acta*, *75*(22), 7257–7276. https://doi.org/10.1016/j.gca.2011.08.007

Sepkoski, J.J., 1995, The Ordovician radiations: diversification and extinction shown by global genus-level taxonomic data, in D. Cooper, M.L. Droser, and S.L. Finney (eds.), Ordovician Odyssey: Short Papers for the Seventh International Symposium on the Ordovician System: Pacific Section Society for Sedimentary Geology (SEPM), Book 77, p. 393–396.

Sheehan, P.M., 2001, The Late Ordovician mass extinction: Annual Review of Earth and Planetary Sciences, v. 29, p. 331–364.

Stone, G. L., & Furnish. (1959). *Bighorn conodonts from Wyoming*.

Sweet, W.C., 1979, Late Ordovician conodonts and biostratigraphy of the Western Midcontinent Province: Brigham Young University Geology Studies, v. 26, p. 45– 85.

Sweet, W.C., 1984, Graphic correlation of upper Middle and Upper Ordovician rocks, North American Midcontinent Province, U.S.A., *in* Bruton, D.L., ed., As- pects of the Ordovician System: Palaeontological Contributions from the Univer- sity of Oslo, Universitetsforlaget, Oslo, p. 23–35.

Torsvik, T. H., Tait, J., Moralev, V. M., McKerrow, W. S., Sturt, B. A., & Roberts, D. (1995). Ordovician palaeogeography of Siberia and adjacent continents. *Journal of the Geological Society*, *152*(2), 279–287. https://doi.org/10.1144/gsjgs.152.2.0279

Tribovillard, N., Algeo, T. J., Lyons, T., & Riboulleau, A. (2006). Trace metals as paleoredox and paleoproductivity proxies: An update. *Chemical Geology*, *232*(1-2), 12–32. https://doi.org/10.1016/j.chemgeo.2006.02.012

Wells, O. C., Gignac, L. M., Murray, C. E., Frye, A., & Bruley, J. (2006). Use of backscattered electron detector arrays for forming backscattered electron images in the scanning electron microscope. *Scanning*, *28*(1), 27–31. https://doi.org/10.1002/sca.4950280105

Wetzel, A., Weissert, H., Schaub, M., & Voegelin, A. R. (2013). Sea-water circulation on an oolite-dominated carbonate system in an epeiric sea (Middle Jurassic, Switzerland). *Sedimentology*, *60*(1), 19–35. https://doi.org/10.1111/sed.12007

Woods, J. D. (1985). Chapter 34 the physics of Thermocline ventilation. *Coupled Ocean-Atmosphere Models*, 543–590. https://doi.org/10.1016/s0422-9894(08)70730-x

Young, S.A., Saltzman, M.R., and Bergström, S.M. 2005. Upper Ordovician (Mohawkian) carbon isotope (δ13C) stratigraphy in eastern and central North America: regional expression of a perturbation of the global carbon cycle. Palaeogeography, Palaeoclimatology, Palaeoecology, **222**: 53–76.

Zenger, D.H., 1992, Burrowing and dolomitization patterns in the Steamboat Point Member, Bighorn Dolomite (Upper Ordovician), northwest Wyoming: Rocky Mountain Geology, v. 29/2, p. 133–142.

Zenger, D.H., 1996, Dolomitization patterns in widespread ‘‘Bighorn Facies’’ (Upper Ordovician), Western Craton, USA: Carbonates and Evaporites, v. 11, p. 219–225, doi: 10.1007/BF03175640.

Figures

Figure 1. Geologic map and stratigraphic column of the Bighorn Dolomite in western Wyoming after Bays et al., 2022.

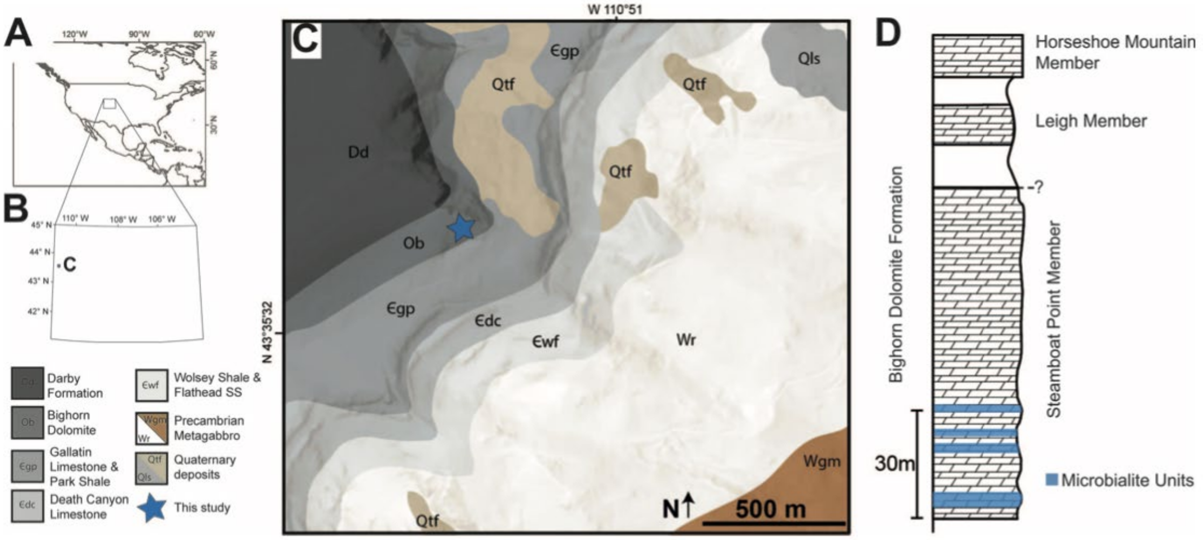

Figure 1. Field site. A, B) Field site location in western Wyoming. C) Geologic map of the field site with star denoting the location where the samples were observed. D)Stratigraphic column of the section at Cody Basin after Zenger (1992).

Figure 2. Paleogeographic map during deposition of the of the Bighorn Dolomite

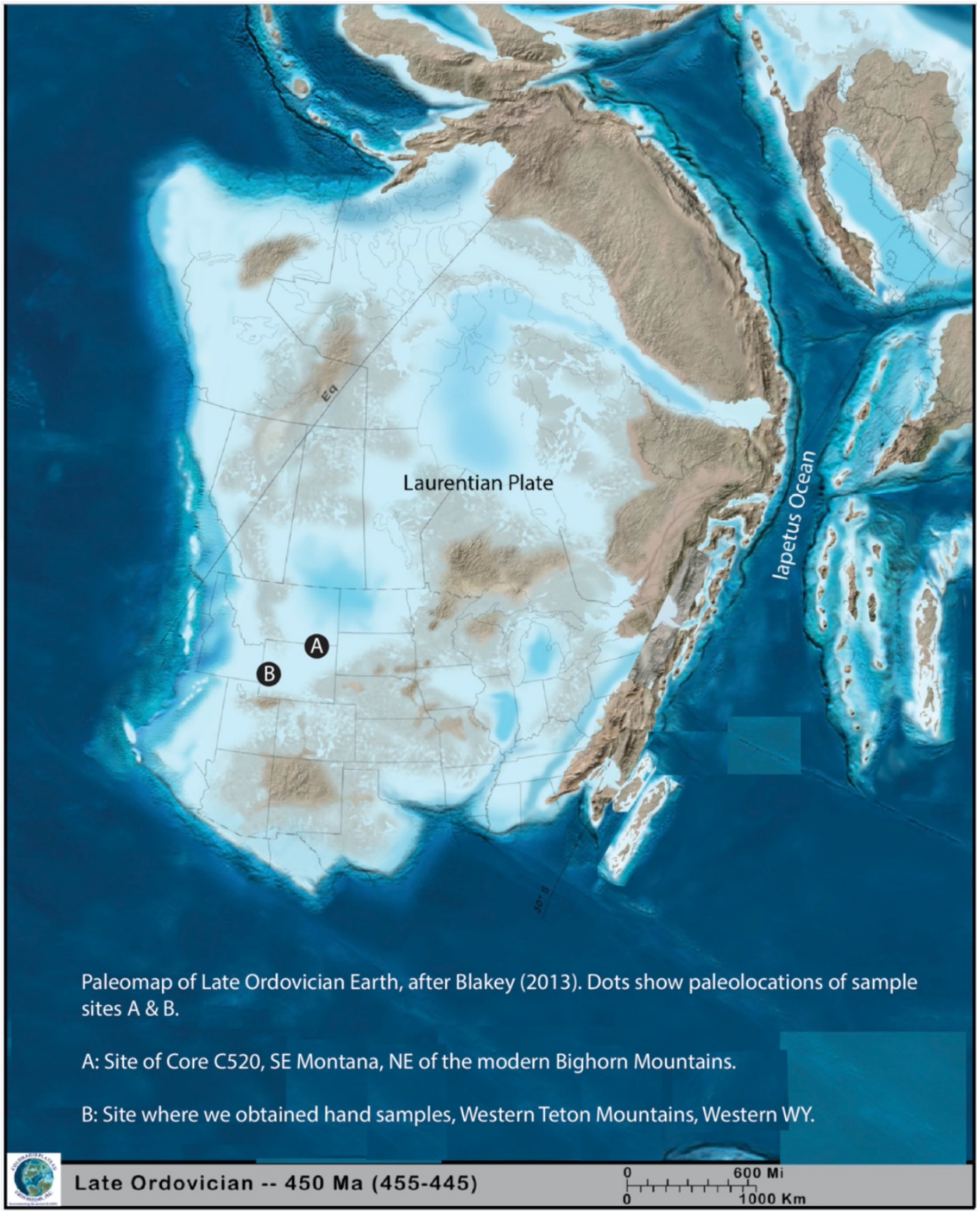

Paleomap of Late Ordovician Earth, after Blakey (2013). Dots show paleolocations of sample sites A & B.

A: Site of Core C520, SE Montana, NE of the modern Bighorn Mountains.

B: Site where we obtained hand samples, Western Teton Mountains, Western WY.

Figure 2. Paleogeographic map of the Laurentia Sea, where the Bighorn Dolomite was deposited during the Late Ordovician. Dots A, B show locations of samples analyzed in this study. Augmented from Blakey (2013).

Figure 3. Ordovician carbonates in the study area

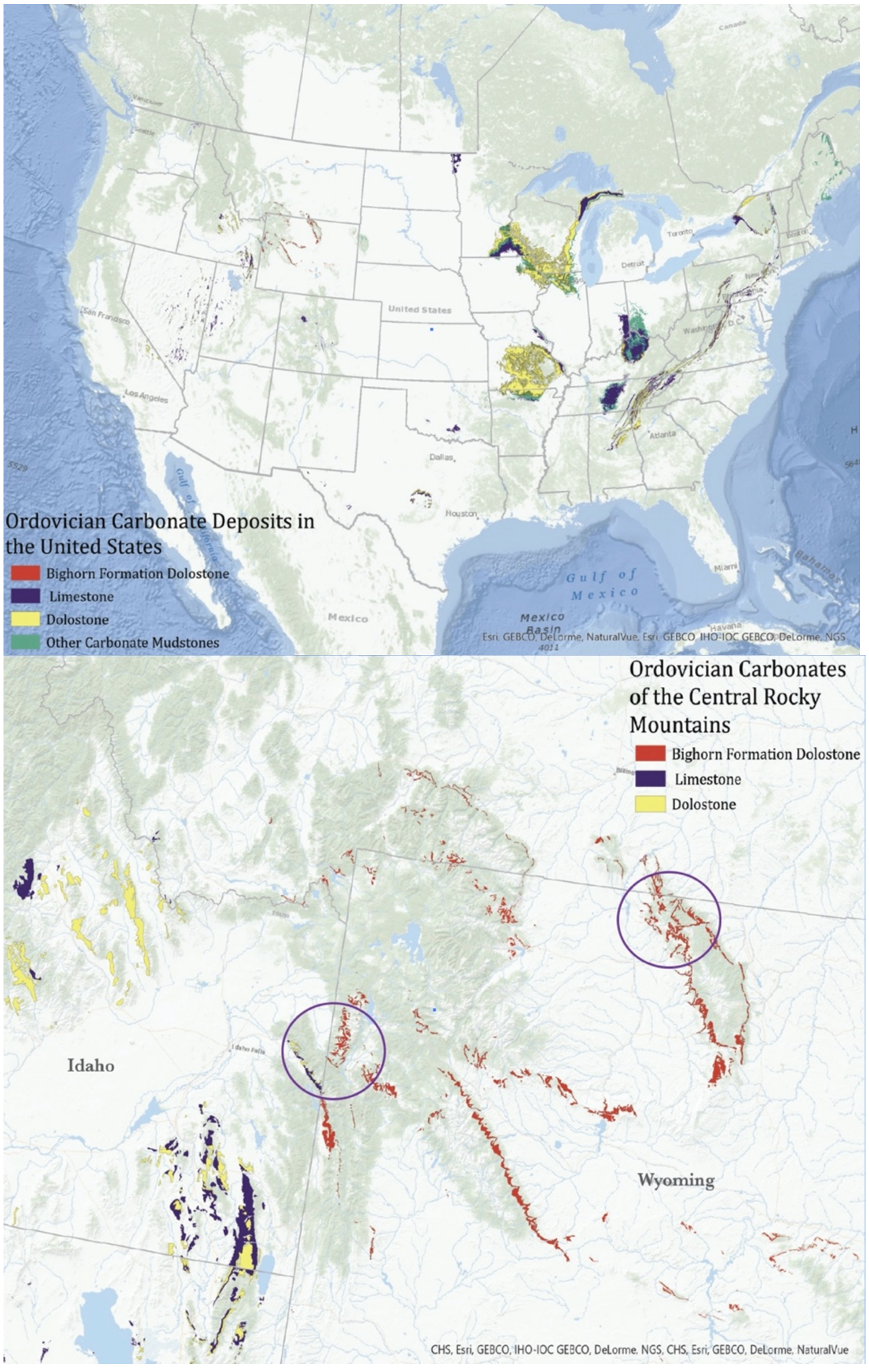

Figure 3. Map showing locations of exposures of Ordovician carbonates in the United States (top), and exposures of Bighorn Dolomite in the Central Rocky Mountains (bottom, in red). Maps made using GIS data.

Figure 4. Four facies of the Steamboat Point Member, from Bighorn Dolomite Core C520

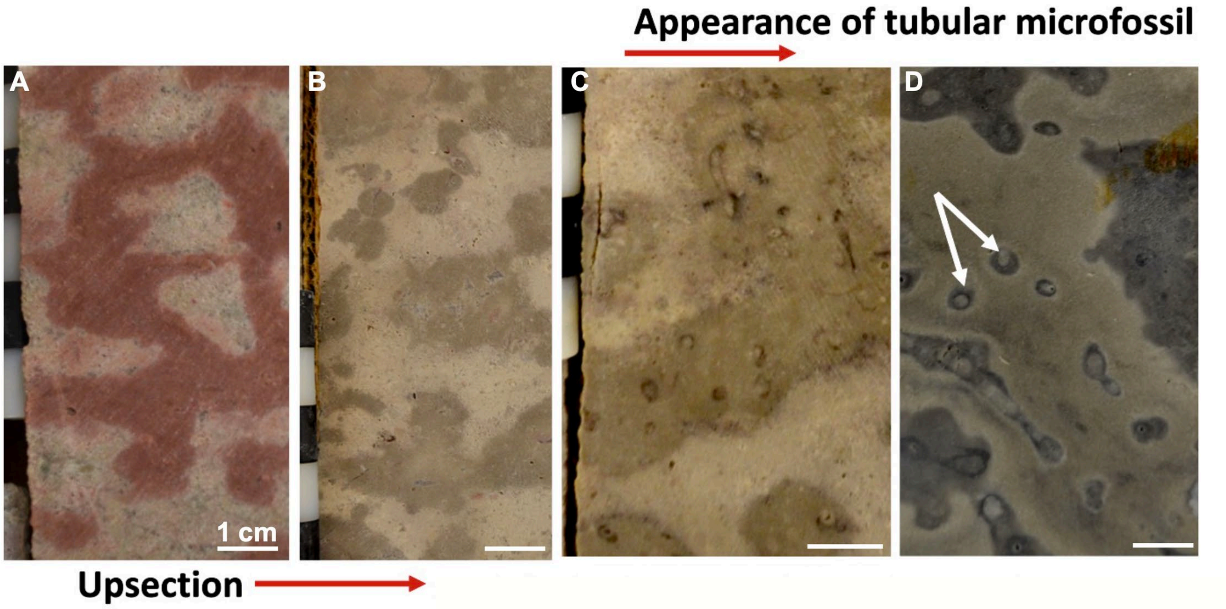

Figure 4. From left to right, the four identified facies changes in the Steamboat Point member of the Bighorn Dolomite: A) Reddish facies; B) Brownish facies; C) Brownish facies with tubular microburrows ;D) Greyish facies with tubular microburrows (arrows). Sampled from core C520. Moving upsection, tubular microburrows appear approximately halfway through the Steamboat Point Member. Tubular fossils and mottles exist independently: together and apart. From left to right: Reddish facies (approx. 9 m.); Brownish facies (approx. 20 m); Brownish facies with microburrows (approx. 30 m); Greyish facies with microburrows (approx. 9 m). All scale bars are 1 cm.

Figure 5. Cross plot of δ^{13}C (VPDB) and depth, from Bighorn Dolomite Core C520

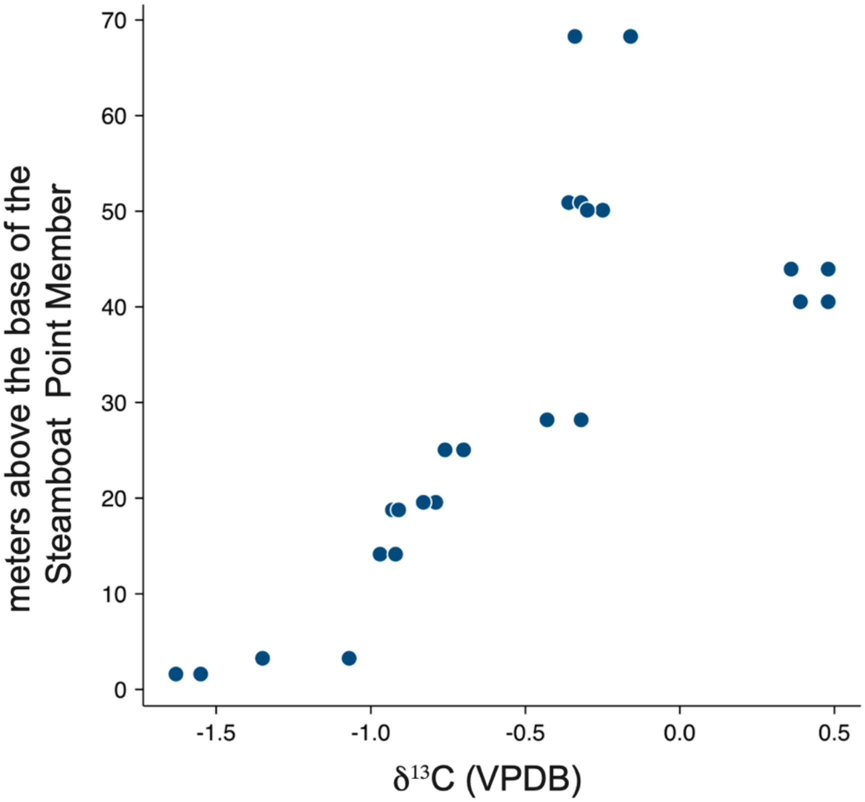

Figure 5. δ^{13}C as a function of depth in the Steamboat Point Member of the Bighorn Dolomite, as sampled from core C520. δ ^{13}C is lower at the bottom of the member and gradually got higher before lowering near the top.

Figure 6. δ^{18}O as a function of depth, from Bighorn Dolomite Core C520

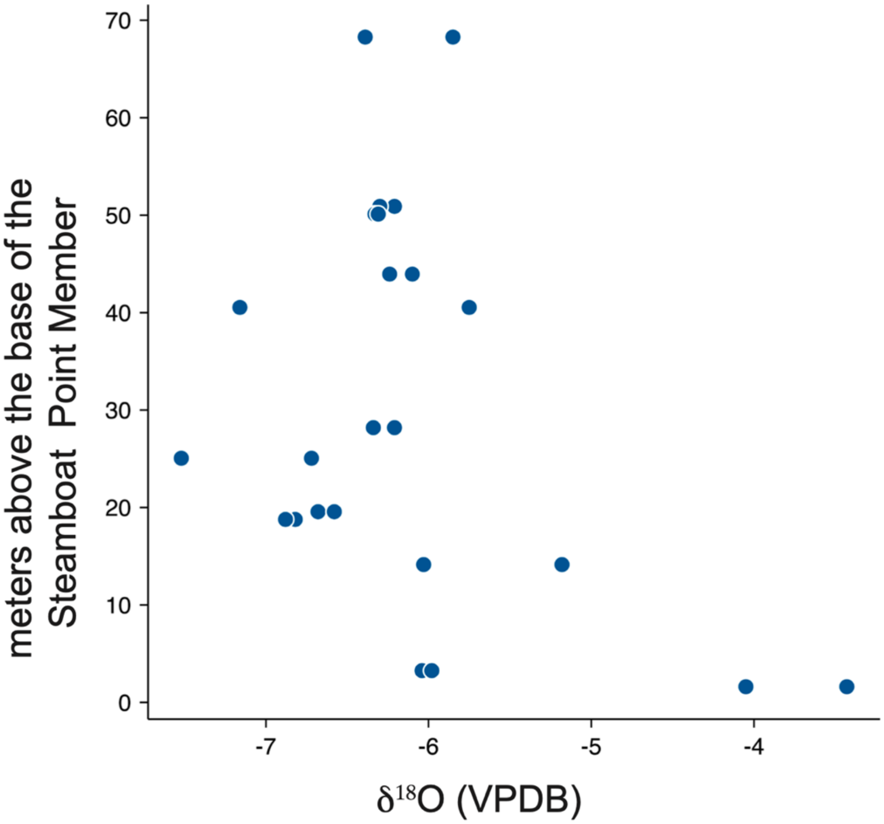

Figure 6. Cross plot of δ^{18}O with depth.

Figure 7. Iron concentration (ppm) as a function of depth, from Bighorn Dolomite Core C520

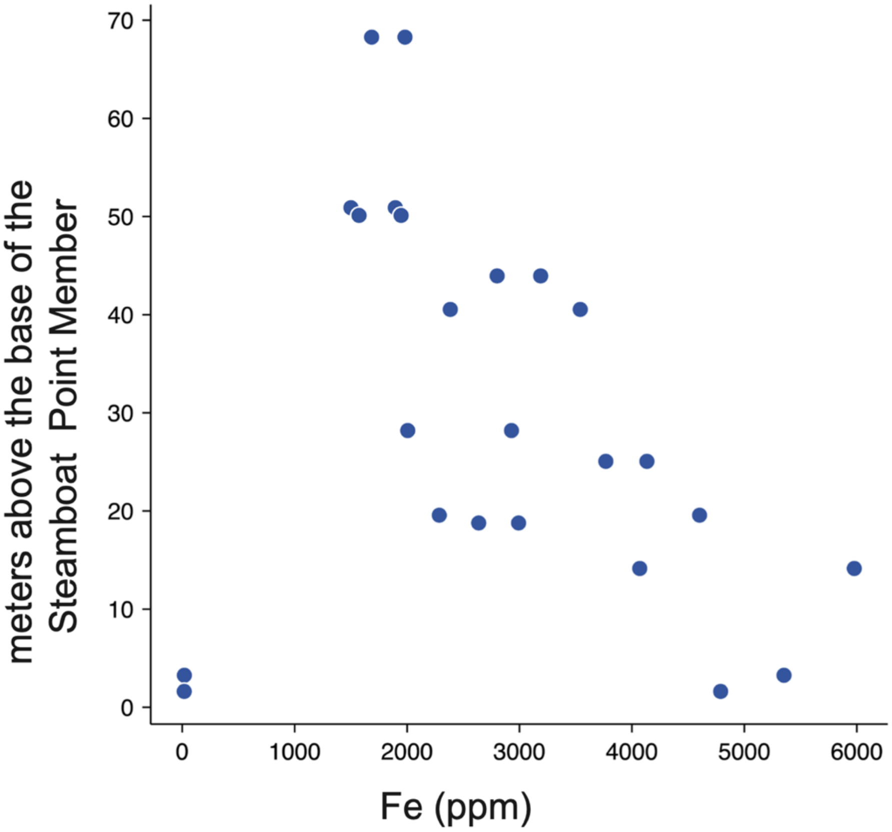

Figure 7. Trace element iron as a function of depth in the Steamboat Point Member of the Bighorn Dolomite. Iron ppm is greater near the bottom of the member and higher near the top.

Figure 8. Manganese concentration (ppm) with depth, from Bighorn Dolomite Core C520

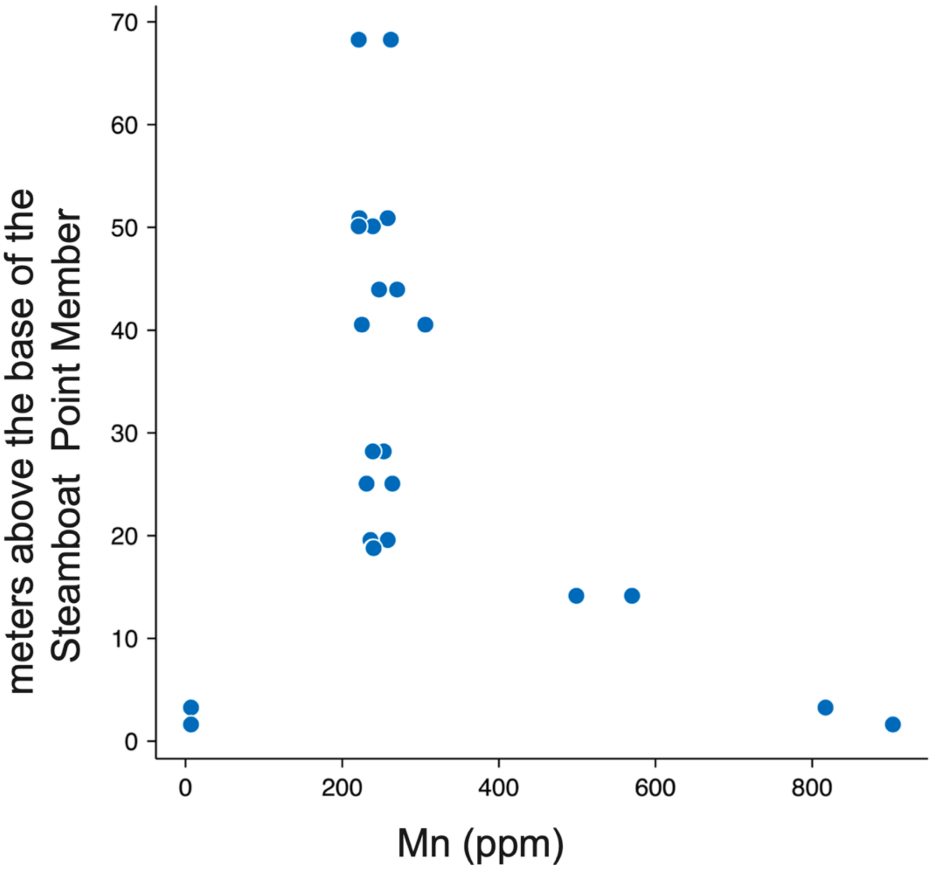

Figure 8. Trace element manganese as a function of depth.

Figure 9. Strontium concentration (ppm) with depth, from Bighorn Dolomite Core C520

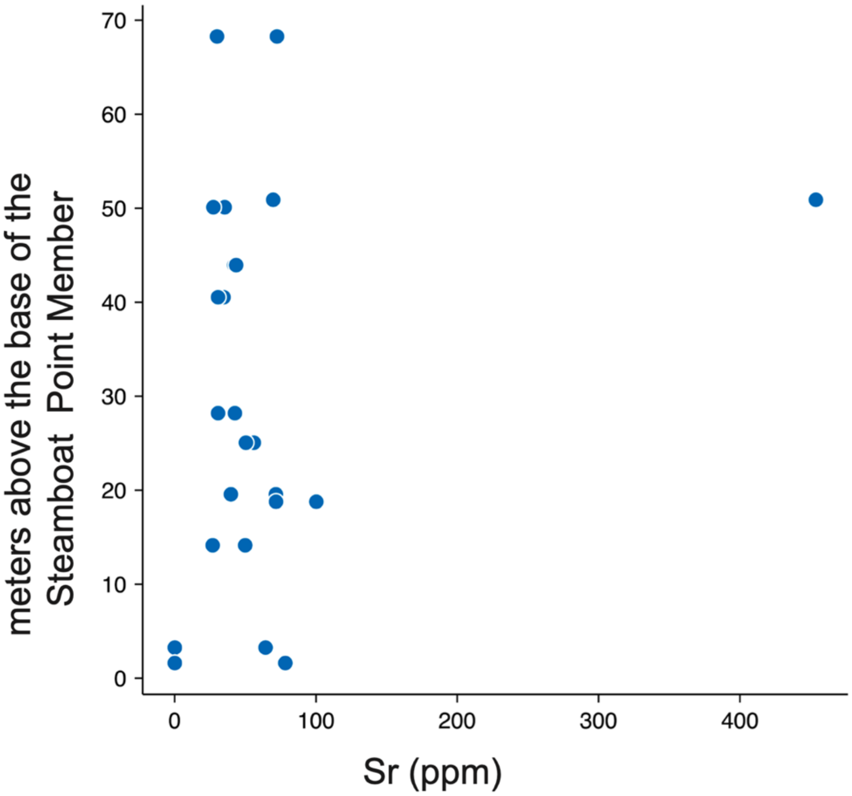

Figure 9. Trace element strontium as a function of depth.

Figure 10. Cross plot of 87Sr/ 86Sr and depth, from Bighorn Dolomite Core C520

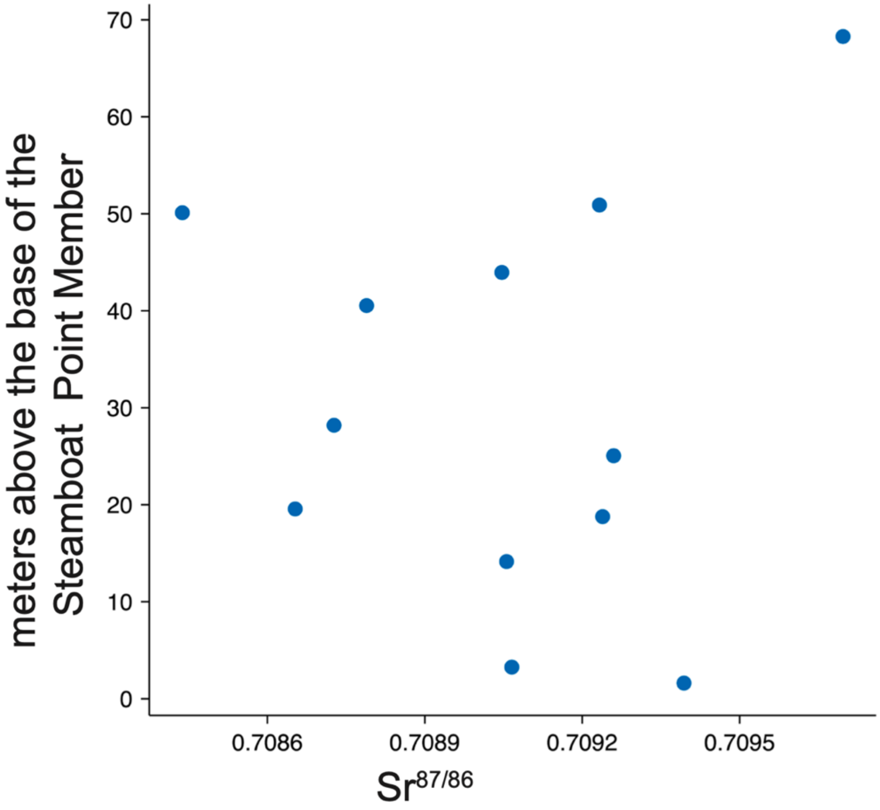

Figure 10. ^{87}*Sr/* ^{86}*Sr as a function of depth in the Steamboat Point member of the Bighorn Dolomite, as sampled from core C520.*

Figure 11. SEM image of Core C520 with EDS analysis points marked

5 keV 25-point analysis of Minerals in C520 sample 1

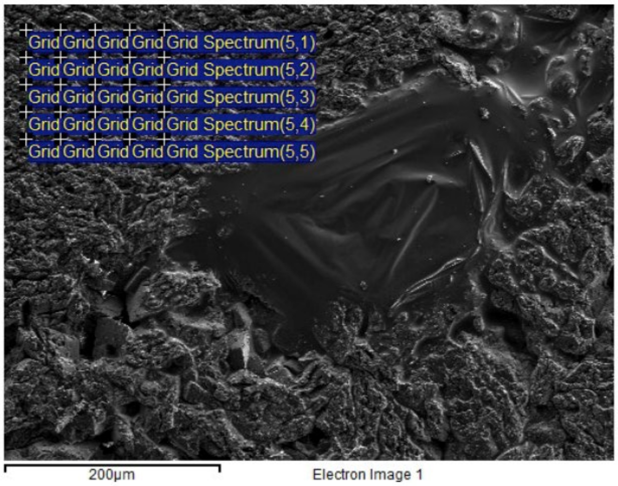

5 keV 25-point analysis of Oil in C520 sample 1 5/2/2022 4:50:28 PM

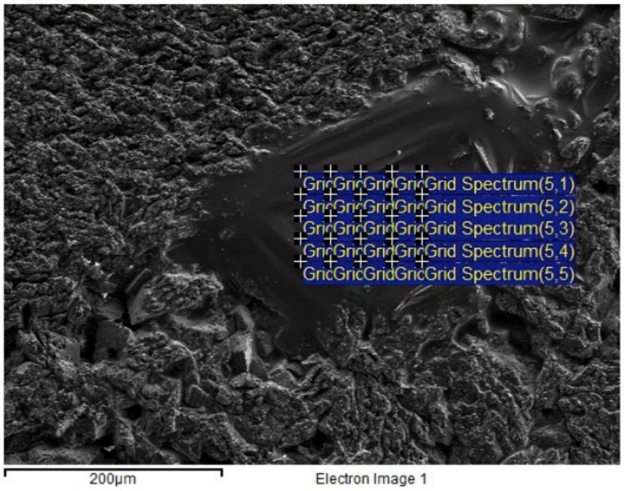

Figure 11. Electron image of Core C520, with locations of the 25-point energy-dispersive X-ray spectroscopy (EDS) analysis. EDS was performed on dolomite (top) and on petroleum (bottom) to attain atomic percentages.

Figure 12. Elemental Composition Tests for ‘Dark Patch’ and Surrounding Dolomite

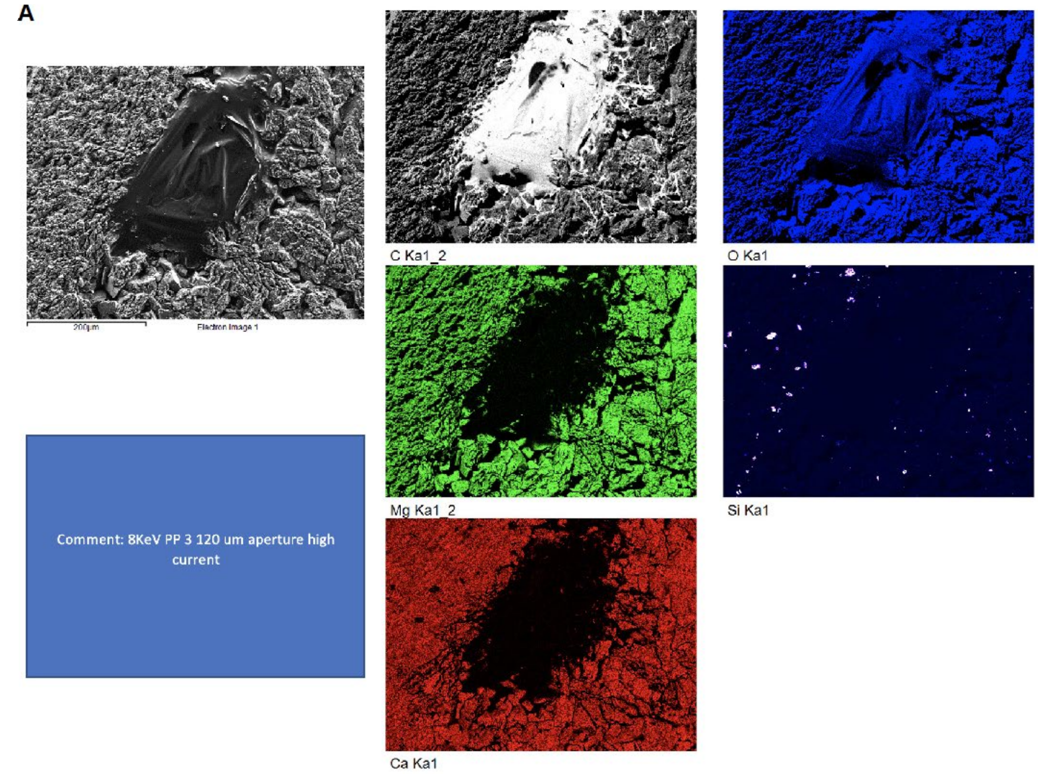

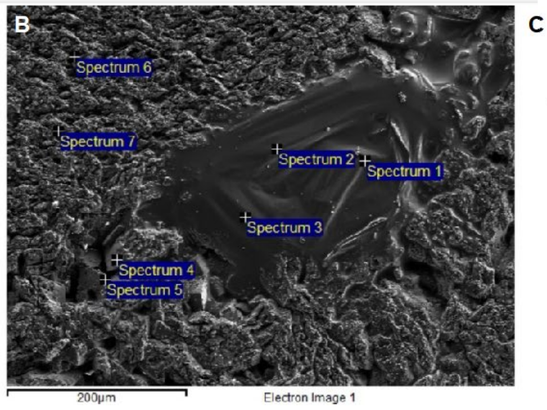

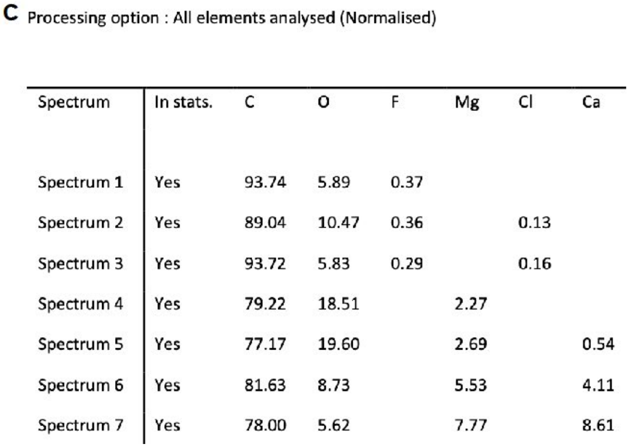
C Processing option : All elements analysed (Normalised)

Spectrum	In stats.	C	O	F	Mg	Cl	Ca
Spectrum 1	Yes	93.74	5.89	0.37			
Spectrum 2	Yes	89.04	10.47	0.36		0.13	
Spectrum 3	Yes	93.72	5.83	0.29		0.16	
Spectrum 4	Yes	79.22	18.51		2.27		
Spectrum 5	Yes	77.17	19.60		2.69		0.54
Spectrum 6	Yes	81.63	8.73		5.53		4.11
Spectrum 7	Yes	78.00	5.62		7.77		8.61

Figure 12. SEM images of a ‘dark patch’ in the Steamboat Point Member of the Bighorn Dolomite. A) Backscattered electron images of the dolomite and ‘dark patch’, with white for calcium, blue for oxygen, green for magnesium, violet for silicon, and red for calcium. Technique outlined in Wells et al., (2006). B) Image of the ‘dark patch’ and surrounding dolomite, with 7 points where EDS measurements were taken. C) EDS results for spectrum points 1-7 for elements carbon, oxygen, fluorine, magnesium, chloride, and calcium.

Figure 13. Millimeter-scale and micrometer-scale images of the two principal fabrics within the Bighorn Dolomite

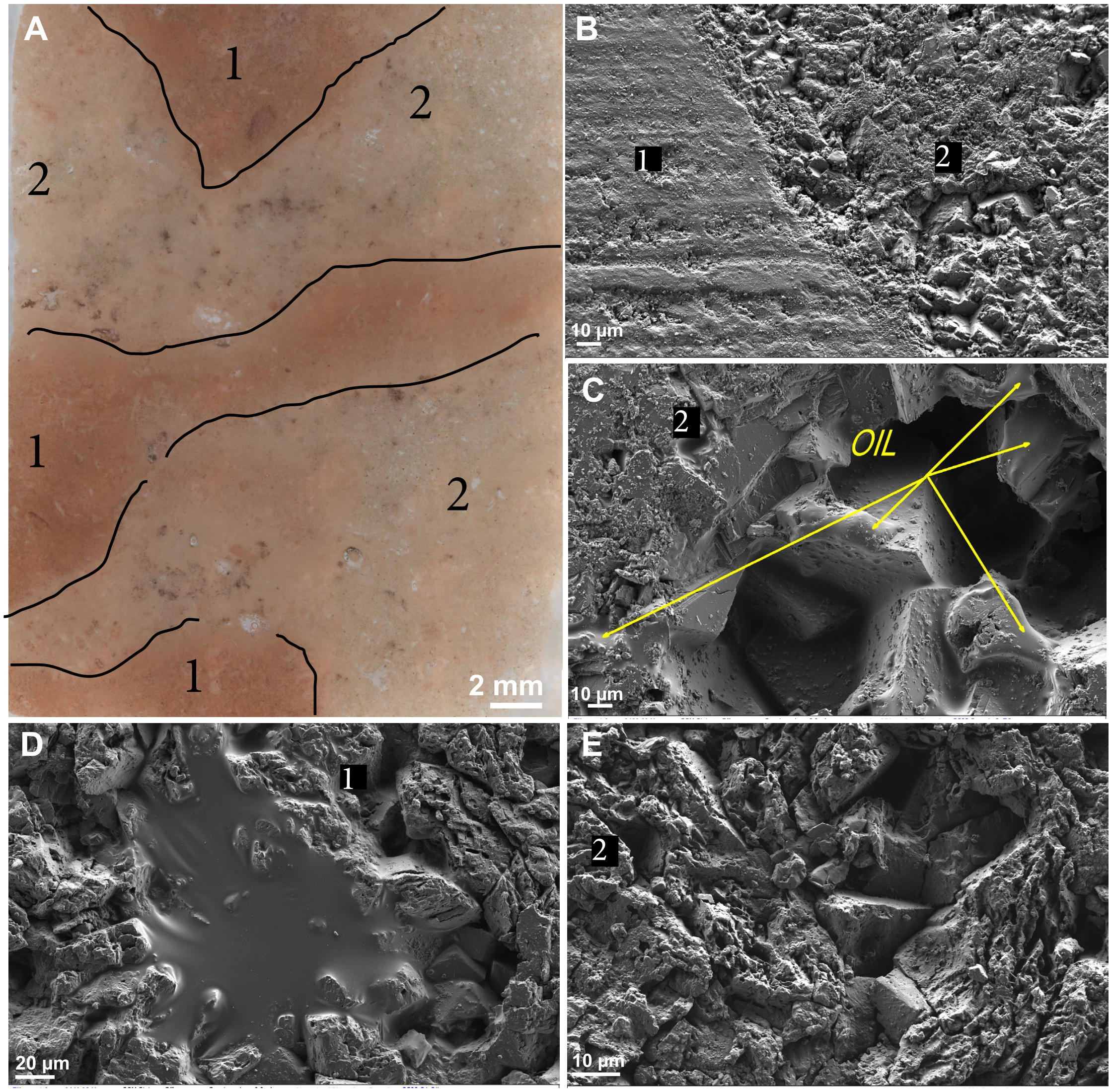

Figure 13. Images at different magnifications of the two fabrics of the Steamboat Point Member. For images A-E, 1= microbial thrombolitic structures. 2= surrounding sediment matrix A) Thin section from the Steamboat Point Member, with a white card placed underneath to illuminate less dense material. B) contrast between finer structure and coarser matrix. C) Micropore within coarse sediment matrix. D) Smooth patch within coarse sediment matrix. E) Microcavities within coarse sediment matrix.

Figure 14. Summary of facies and geochemical analyses of the Bighorn Dolomite

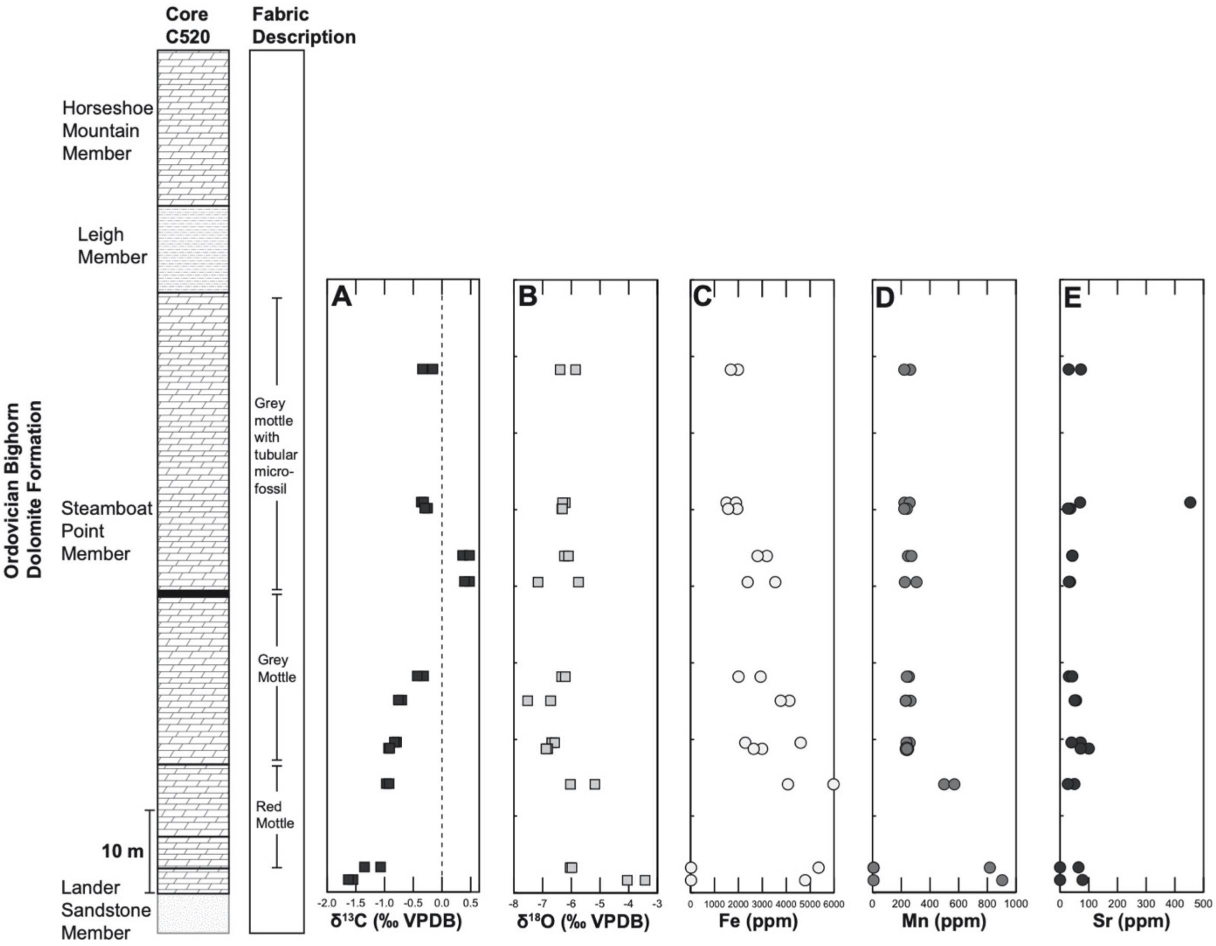

Figure 14. Stratigraphic column of Bighorn Dolomite on the left with geochemical and facies descriptions as a function of depth in the Steamboat Point Member. Fabric description column shows facies evolution of the Steamboat Point Member. A) $\delta^{13}C$ *(VPDB) B)* $\delta^{18}O$ *(VPDB) C) Fe ppm D) Mn ppm E) Sr ppm.*

Figure 15. Model for sea level forcing of δ^{13}C in the depositional environment of the Bighorn Dolomite

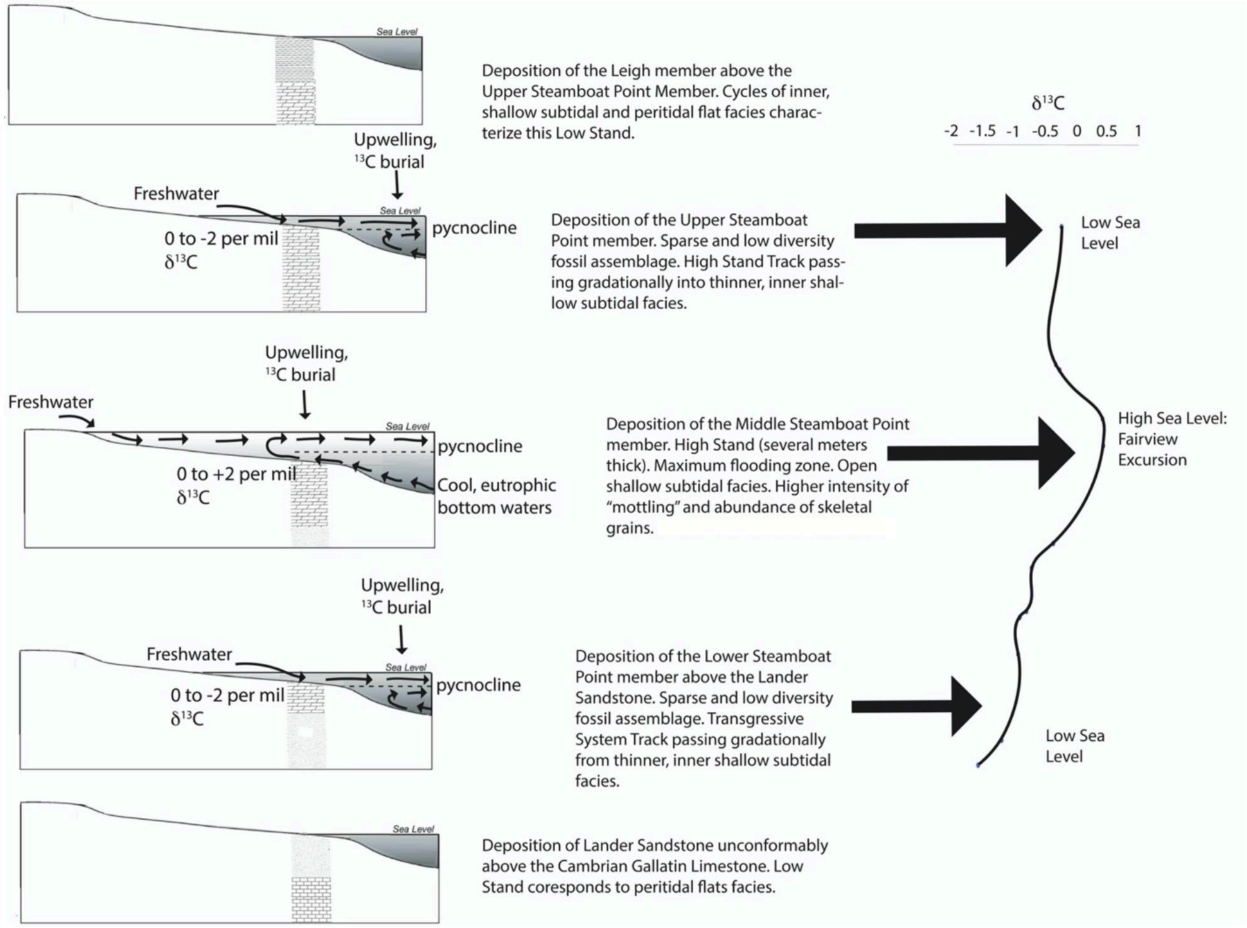

Figure 15. The quasiestuarine circulation model for distribution of δ^{13}C, from Fanton & Holmden (2007). Deposition is conceptualized by the vertical band displayed on the shelf, and facies environments are from Holland & Patzkowsky (2009). The basic idea of the quasiestuarine circulation model is that higher ^{13}C is concentrated below the pycnocline, where density increases. At the bottom, corresponding to the stratigraphic lower boundary of the Steamboat Point member of the Bighorn Dolomite, the shallow water depositional environment of the Lander Sandstone. Above the Lander Sandstone, the lower Steamboat Point member was deposited under inner shallow subtidal facies. The middle Steamboat Point was deposited under deeper water, probably open shallow subtidal facies. The upper Steamboat Point was deposited in a similar environment to the lower Steamboat Point, i.e. inner shallow subtidal facies.

.

Figure 16. Composite δ^{13}C curves for the Katian, from Jing et al. (2019)

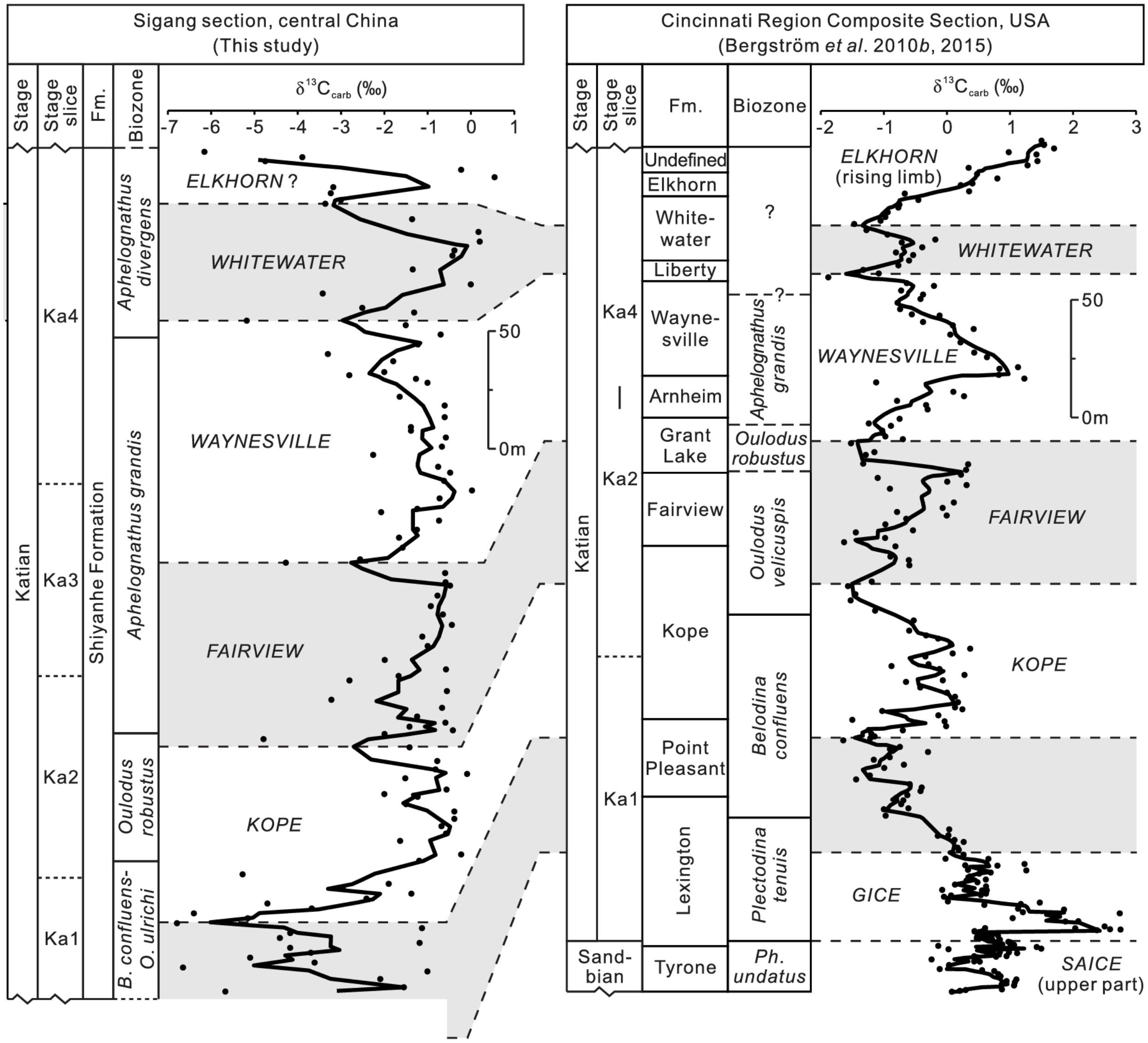

Figure 16. δ^{13}C excursion profile of the Sigang region, Central China (left), and the Cincinnati region (right), from Jing et al. (2019). The Fairview excursion occurs in the Oulodus velicuspis to Oulodus robustus conodont zones in North america, which Holland & Patzkowsky (2009) attribute to the Steamboat Point member of the Bighorn Dolomite. The amplitude of the excursion shown is comparable to the excursion found in this study.

Figure 17. Composite δ^{13}C curve for the Katian, from Bergström et al. (2010)

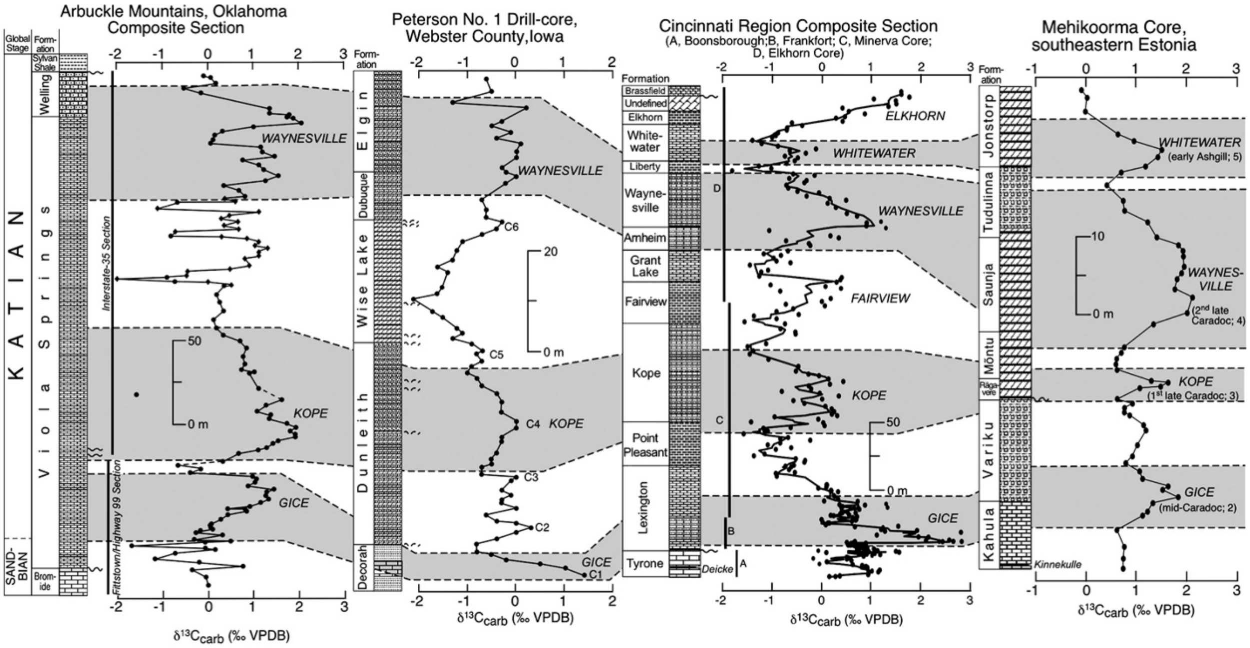

Figure 17. δ^{13}C excursion profile of Katian rocks from Oklahoma, Iowa, Cincinnati region, and Estonia (Bergström et al., 2010). The Fairview excursion is shown to a greater or lesser extent among global rocks. The amplitude of the excursion shown is comparable to the excursion found in this study.

Figure 18. Oxygen isotopes for Paleozoic carbonates

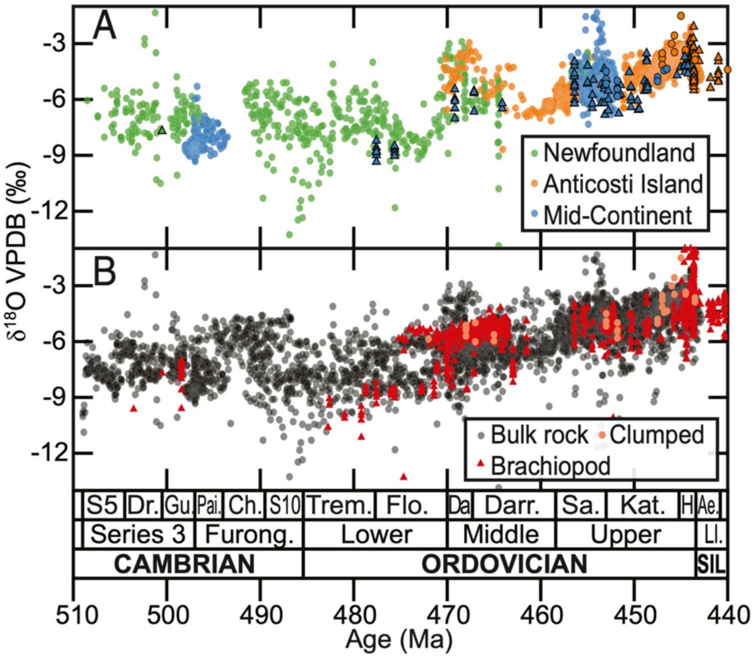

Figure 18. Oxygen Isotope Data for the Paleozoic (Goldberg et al. 2021). Our results show an average of -6.09, which is within the values shown for the Katian.

Figure 19. Carbon and oxygen stable isotope data from Bighorn Dolomite Core C520

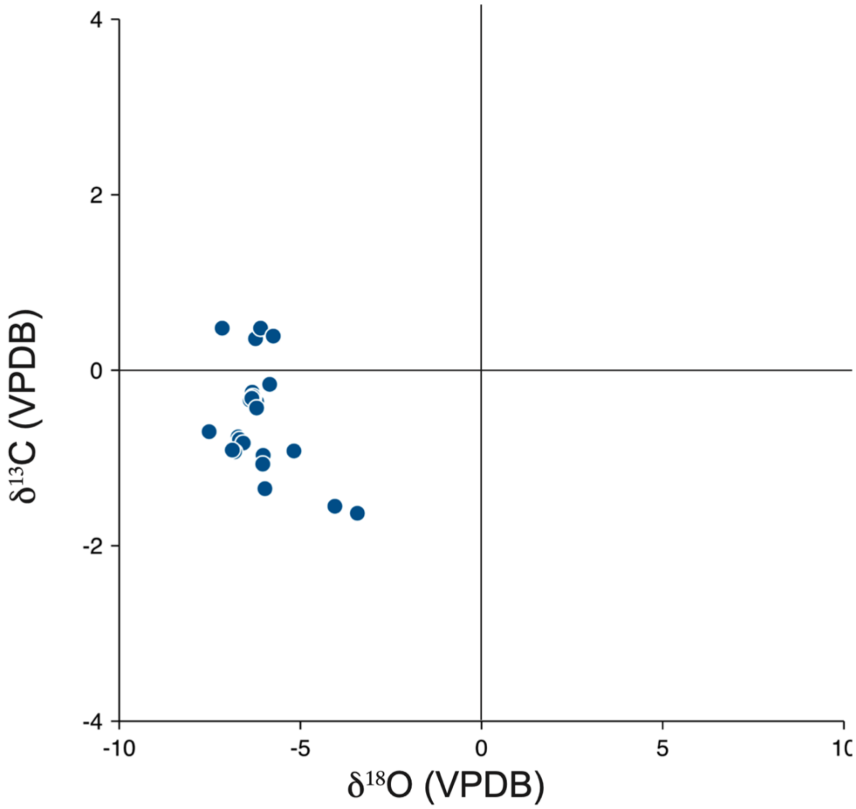

Figure 19. Cross plot of $\delta^{13}C$ *and* $\delta^{18}O$ *in the Bighorn Dolomite. The majority of values occur within the sulfate-reduction field for authigenic dolomites (James & Jones, 2016).*

Figure 20. Cross plot of Strontium concentration (ppm) and 87Sr/86Sr, from Bighorn Dolomite Core C520

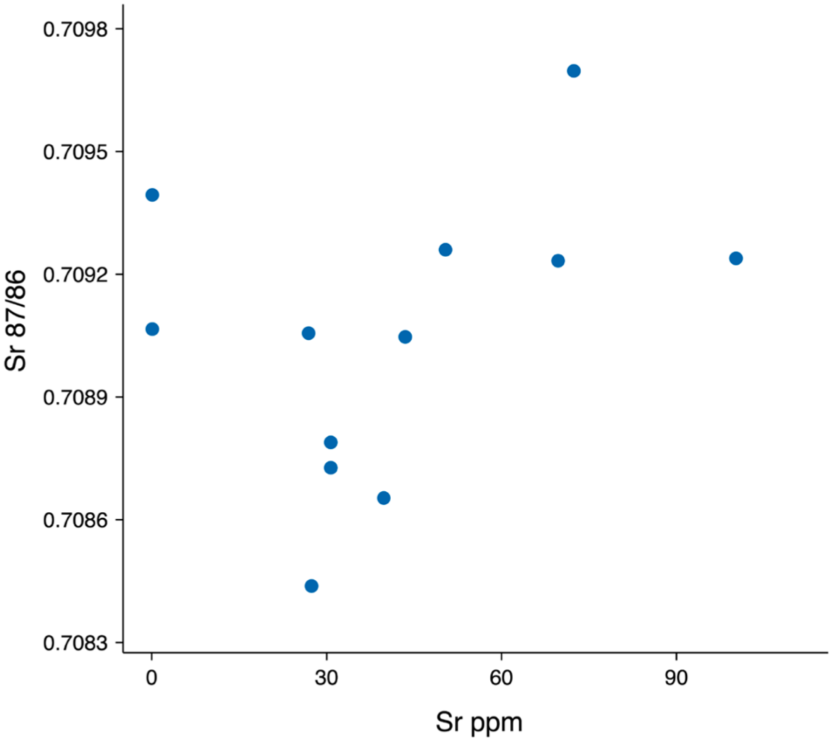

Figure 20. Strontium ppm versus the isotopic ratio $^{87}Sr/^{86}Sr$*. The correlation probably indicates strontium diagenesis (Banner, 1995).*

Tables

Table 1. Carbon and oxygen stable isotope data from Bighorn Dolomite Core C520

Depth (ft.)	Depth (m)	δ^{13}C (‰ VPDB)	SD of vial (^{13}C)	δ^{18O} (‰ VPDB)	SD of vial (^{18}O)
11634.1	3546.04	-0.34	0.07	-6.39	0.09
11634.1	3546.04	-0.16	0.02	-5.85	0.07
11691.2	3563.42	-0.36	0.04	-6.21	0.05
11691.2	3563.42	-0.32	0.05	-6.3	0.05
11693.6	3564.21	-0.25	0.04	-6.33	0.08
11693.6	3564.21	-0.3	0.03	-6.31	0.02
11713.8	3570.37	0.36	0.01	-6.24	0.03
11713.8	3570.37	0.48	0.03	-6.1	0.07
11725	3573.78	0.48	0.08	-7.16	0.03
11725	3573.78	0.39	0.04	-5.75	0.07
11769.5	3586.12	-0.32	0.06	-6.34	0.05
11765.5	3586.12	-0.43	0.03	-6.21	0.07
11775.8	3589.26	-0.7	0.05	-7.52	0.07
11775.8	3589.26	-0.76	0.02	-6.72	0.06
11793.8	3594.75	-0.79	0.02	-6.68	0.06
11793.8	3594.75	-0.83	0.03	-6.58	0.05
11796.4	3595.54	-0.93	0.02	-6.82	0.07
11796.4	3595.54	-0.91	0.02	-6.88	0.05
11811.6	3600.18	-0.97	0.02	-6.03	0.04
11811.6	3600.18	-0.92	0.02	-5.18	0.05
11847.3	3611.06	-1.07	0.06	-6.04	0.06
11847.3	3611.06	-1.35	0.02	-5.98	0.07
11852.7	3612.70	-1.55	0.04	-4.05	0.02
11852.7	3612.70	-1.63	0.04	-3.43	0.03
11879.8	Lander SS				
11879.8	Lander SS				
11908.8	Lander SS				
11908.8	Lander SS				

Teton Exposure 1	N/A	-0.27	0.03	-5.98	0.05
Teton Exposure 2	N/A	-0.26	0.03	-5.87	0.05
Teton Exposure 3	N/A	-0.16	0.04	-6.01	0.08
Teton Exposure 4	N/A	-0.25	0.03	-6.16	0.03
Teton Exposure 5	N/A	-0.32	0.04	-6.01	0.06
Teton Exposure 6	N/A	-0.25	0.05	-6.08	0.05
Teton Exposure 7	N/A	-0.14	0.02	-6.08	0.06
Teton Exposure 8	N/A	-0.02	0.02	-5.93	0.04
Teton Exposure 9	N/A	-0.24	0.06	-5.97	0.09
Teton Exposure 10	N/A	-0.35	0.02	-5.99	0.06

Table 1. $d^{13}C$, $d^{18}O$, and standard deviations at different depths of sampling in the Steamboat Point member of the Bighorn Dolomite (Core C520, USGS Core Research Center).

Table 2. Trace element data from Bighorn Dolomite Core C520

Depth (ft.)	Depth (m)	Mn ppm	Fe ppm	Sr ppm
11634.1	3546.04	262	1981	30
11634.1	3546.04	221	1685	72.4
11691.2	3563.42	222	1500	453.7
11691.2	3563.42	258	1895	69.7
11693.6	3564.21	239	1946	35.4
11693.6	3564.21	221	1572	27.4
11713.8	3570.37	247	3189	42.1
11713.8	3570.37	270	2801	43.5
11725	3573.78	225	3540	34.6
11725	3573.78	306	2385	30.7
11769.5	3586.12	253	2929	30.7
11765.5	3586.12	239	2005	42.6
11775.8	3589.26	264	4133	56
11775.8	3589.26	231	3768	50.4
11793.8	3594.75	258	4602	71.6
11793.8	3594.75	236	2287	39.8
11796.4	3595.54	239	2992	100.2
11796.4	3595.54	240	2638	71.7
11811.6	3600.18	499	5977	49.9
11811.6	3600.18	570	4070	26.9
11847.3	3611.06	817	5352	64.3
11847.3	3611.06	7	19	0.1
11852.7	3612.70	903	4789	78.3
11852.7	3612.70	7	18	0.1
11879.8	Lander SS	195	46093	93.9
11879.8	Lander SS	175	45772	53.2
11908.8	Lander SS	15	2383	22.2
11908.8	Lander SS	51	13973	27.1
Teton Exposure 1		45	414	23.7
Teton Exposure 2		53	539	27.3
Teton Exposure 3		52	383	24.3

Teton Exposure 4		49	434	26.7
Teton Exposure 5		47	380	26.4
Teton Exposure 6		45	356	27.9
Teton Exposure 7		55	458	27.6
Teton Exposure 8		89	458	24.9
Teton Exposure 9		44	334	24.8
Teton Exposure 10		42	362	26.8

Table 2. Iron, Manganese, and Strontium concentrations (ppm) at different depths of sampling in the Steamboat Point member of the Bighorn Dolomite (Core C520, USGS Core Research Center).

Table 3. Strontium isotope ratio data from Bighorn Dolomite Core C520

Depth (ft.)	Depth (m)	Sr 87/86	Sr 84/86	Sr 86/88
11634.1	3546.04			
11634.1	3546.04	0.709697	0.056501	0.114463
11691.2	3563.42			
11691.2	3563.42	0.709233	0.056499	0.114458
11693.6	3564.21			
11693.6	3564.21	0.708438	0.056497	0.114462
11713.8	3570.37			
11713.8	3570.37	0.709047	0.0565	0.114472
11725	3573.78			
11725	3573.78	0.708789	0.056492	0.114435
11769.5	3586.12	0.708727	0.056507	0.114429
11765.5	3586.12			
11775.8	3589.26			
11775.8	3589.26	0.70926	0.056515	0.114417
11793.8	3594.75			
11793.8	3594.75	0.708653	0.05646	0.114394
11796.4	3595.54	0.709239	0.056511	0.114415
11796.4	3595.54			
11811.6	3600.18			
11811.6	3600.18	0.709056	0.056481	0.114349
11847.3	3611.06			
11847.3	3611.06	0.709066	0.056467	0.114357
11852.7	3612.70			
11852.7	3612.70	0.709394	0.056501	0.114359
11879.8	Lander SS			
11879.8	Lander SS			
11908.8	Lander SS			
11908.8	Lander SS			
Teton Exposure 1		0.708778	0.05651	0.114385

Teton Exposure 2				
Teton Exposure 3				
Teton Exposure 4				
Teton Exposure 5				
Teton Exposure 6				
Teton Exposure 7				
Teton Exposure 8				
Teton Exposure 9		0.708749	0.056485	0.11436
Teton Exposure 10				

Table 3. Strontium isotope ratios at different depths of sampling in the Steamboat Point Member of the Bighorn Dolomite (Core C520, USGS Core Research Center).

Table 4. 25-point analysis of atomic % of elements in Dolomite in C520 sample 1

Point	C %	O %	Mg %	Ca %
1	85.23	11.80	2.40	0.57
2	86.96	11.68	1.05	0.31
3	87.64	9.46	2.38	0.52
4	75.75	12.73	6.86	4.66
5	66.96	10.76	1.71	20.57
6	50.58	11.10	22.29	16.04
7	45.86	3.94	22.01	28.19
8	94.07	5.72	0.21	0.0
9	72.74	23.19	2.86	1.22
10	85.32	6.45	6.48	1.74
11	96.90	0.00	3.10	0.00
12	94.83	2.92	1.53	0.72
13	89.71	8.95	0.96	0.38
14	81.37	16.07	2.10	0.45
15	94.56	3.26	2.18	0.00
16	47.88	4.92	12.03	35.18
17	80.23	14.63	3.93	1.22
18	80.05	18.44	1.31	0.21
19	79.36	8.77	6.81	5.06
20	71.07	23.18	3.81	1.94
21	79.53	13.79	5.27	1.41
22	89.55	10.04	0.41	0.00
23	73.46	18.99	5.73	1.82
24	88.59	7.14	3.31	0.96
25	63.32	25.91	5.98	4.79

Table 4. EDS analysis of atomic % of elements in dolomite in sample from Core C520. Elements detected are carbon, oxygen, magnesium, calcium. All elements normalized.

Table 5. 25-point analysis of atomic % of elements in 'dark patches' in C520 sample 1

Point	C %	O %	F %	Cl %
1	92.63	6.95	0.30	0.1
2	91.70	7.94	0.35	0.00
3	98.60	0.86	0.09	0.45
4	91.94	7.79	0.28	0.00
5	90.65	8.52	0.69	0.13
6	92.50	7.09	0.24	0.17
7	95.99	3.56	0.30	0.15
8	89.98	9.51	0.41	0.1
9	93.38	6.08	0.46	0.08
10	92.11	7.15	0.63	0.11
11	93.09	6.53	0.21	0.17
12	92.74	6.81	0.34	0.11
13	94.32	5.17	0.38	0.14
14	92.53	6.91	0.45	0.11
15	92.77	6.59	0.49	0.15
16	85.27	14.37	0.30	0.07
17	85.54	13.80	0.52	0.15
18	87.63	11.81	0.36	0.21
19	90.67	8.87	0.36	0.10
20	90.26	9.02	0.59	0.13
21	92.70	6.90	0.23	0.17
22	83.09	16.37	0.47	0.07
23	84.58	14.32	0.41	0.69
24	91.56	7.85	0.45	0.14
25	92.04	7.42	0.35	0.2

Table 5. EDS analysis of atomic % of elements in organic-rich sample from Core C520. Elements detected are carbon, oxygen, fluorine, chloride. All elements normalized.